land

Article

Operational Multi-Source Data Fusion for High-Resolution LULC Mapping

Claudia Collu [1,2,*], Dario Simonetti [3], Francesco Dessì [1], Hugo Iker Gael Gómez Diez [1], Alberto Masala [4], Pasquale Lasio [5], Paolo Botti [5] and Maria Teresa Melis [1]

[1] Department of Chemical and Geological Sciences, University of Cagliari, 09042 Monserrato, Italy; fdessi@unica.it (F.D.); h.gomezdiez@studenti.unica.it (H.I.G.G.D.); titimelis@unica.it (M.T.M.)
[2] Department of Civil, Constructional and Environmental Engineering, Sapienza University of Rome, 00184 Rome, Italy
[3] Independent Researcher, 21100 Varese, Italy; gis.dario.simonetti@gmail.com
[4] Sky Survey System di Alberto Masala & C. S.A.S., 09047 Selargius, Italy; info@skyss.it
[5] Directorate General of the Regional Agency of the Hydrographic District of Sardinia, Via Mameli 88, 09123 Cagliari, Italy; plasio@regione.sardegna.it (P.L.); pbotti@regione.sardegna.it (P.B.)
* Correspondence: claudia.collu@uniroma1.it

Abstract

High-resolution and regularly updatable land cover maps are essential for local-scale environmental monitoring, water resource management, and territorial governance, yet existing global and regional products fail to provide the spatial detail and thematic richness required for operational applications in complex Mediterranean landscapes. This study presents an operational workflow for high-resolution LULC mapping and its application to Sardinia for the reference year 2020, developed within the Sardinia Land Cover Mapping Project in collaboration with the Agenzia del Distretto Idrografico della Sardegna (ADIS). The workflow integrates multi-temporal SAR and multispectral satellite imagery with high-resolution ancillary geospatial vector datasets through a semi-automatic pipeline combining hierarchical cascade pixel-based classification, multi-resolution image segmentation, geometric overlay of infrastructure vector layers, and an iterative accuracy-driven reclassification cycle. The classification combines automated rule-based procedures, semi-automatic threshold-based methods, and expert photo-interpretation to address the high thematic and spatial complexity of the Sardinian landscape. The resulting map comprises 35 land cover classes at the third and selected fourth CORINE levels, with a minimum mapping unit of 400 m^2 and an overall weighted accuracy of 82.4%. Designed as a dynamic product updatable on an annual basis, it represents an operational tool for local environmental governance, spatial planning, and resource management.

Keywords: LULC mapping; CORINE Land Cover; Sentinel-1; Sentinel-2; Google Earth Engine; image segmentation; accuracy assessment; Mediterranean; land use; land cover

Academic Editor: Hikmet Gunal

Received: 4 June 2026
Revised: 10 August 2026
Accepted: 12 August 2026
Published: 13 August 2026

1. Introduction

Land cover and land use (LULC) mapping represents a fundamental component of environmental monitoring, spatial planning, and land management. It supports a wide range of applications, including disaster risk reduction, urban and regional planning, climate change impact assessment, and agricultural monitoring, by providing essential information on land dynamics, crop conditions and water state to optimize resource management and reduce environmental pressures [1–4]. In recent years, the increasing availability of Earth observation data, particularly from the Sentinel missions, and advances in computing, capable of handling large volumes of data, have significantly improved the potential for generating high-resolution and frequently updated LULC products [5–7].

Despite these advancements, the transition from experimental frameworks to operational applications at regional and local scales remains challenging [8]. In real-world contexts, classification performance is affected by increased spatial, temporal, and thematic complexity, especially in heterogeneous landscapes characterized by high fragmentation and variability. These conditions reduce class separability and lead to less stable and more context-dependent classification results, highlighting a persistent gap between methodological developments and operational mapping requirements [5].

Several approaches have been developed to address LULC classification, each with specific advantages and limitations, from traditional visual photointerpretation, which is accurate but time-consuming and difficult to scale, to rule-based classifiers [9–12], supervised machine learning [13–16], Object-Based Image Analysis [4,17,18], and deep learning techniques [19–21]. No single method can fully address the complexity of LULC mapping in real-world conditions; the integration of multiple approaches and heterogeneous data sources represents the most robust strategy in complex territorial settings [22–26].

These methodological challenges are directly reflected in the characteristics of currently available land cover products. Global datasets such as ESA WorldCover [27], S2GLC [28], and GLC_FCS10 [6] provide spatially consistent information but often lack the thematic detail required for local governance applications. CLC2018 [29] offers a semantically rich classification scheme but is characterized by a coarse minimum mapping unit incompatible with local-scale analysis. At the national scale, De Fioravante et al. [30] produced a 10 m raster land cover map of Italy, achieving 83% overall accuracy across 16 EAGLE-compliant classes, demonstrating the feasibility of high-resolution national mapping, but with thematic detail insufficient for local governance requiring CORINE-level distinctions.

A further issue concerns the distinction between land cover and land use. While multispectral satellite data are highly effective in capturing biophysical properties of the surface, they are inherently less capable of representing functional and socio-economic aspects that define land use classes. This limitation becomes particularly relevant when adopting standardized classification systems such as CORINE Land Cover, where several classes are defined not only by physical characteristics but also by their functional role [31].

In Sardinia, the most recent regional land use map dates to 2008 [32,33], produced through expert photointerpretation at 1:25,000 scale with a minimum mapping unit of 0.5–0.75 ha and 71 classes. Despite its exceptional thematic detail, this product has not been updated in over eighteen years, leaving a significant gap during a period of substantial landscape change including wildfire disturbance, agricultural abandonment, and urban expansion. No existing global, continental, or national product simultaneously satisfies the spatial resolution, thematic detail, temporal currency, and updatability requirements for operational land management at the local scale in Sardinia, a territory characterized by exceptional environmental heterogeneity, fragmented agricultural mosaics, complex wetland systems, and high wildfire risk that represent specific and well-documented challenges for spectral classification.

In this context, this study presents a methodology and its application for high-resolution LULC mapping in Sardinia, developed within the "Sardinia Land Cover Mapping Project" in collaboration with the Agenzia del Distretto Idrografico della Sardegna (ADIS). The primary methodological contribution is an operational workflow architecture and annual updatability, specifically designed to produce thematically rich LULC maps in complex heterogeneous landscapes where a pre-existing labelled training dataset is unavailable. The approach combines supervised machine learning, automated rule-based procedures, and expert photointerpretation to exploit their complementary strengths, ensuring scalability, thematic consistency, and operational applicability for local environmental governance and regular annual updates.

2. Study Area

Sardinia is the second-largest island in the Mediterranean Sea (Figure 1), covering an area of approximately 24,098 km^2 and located at the center of its western basin, between 38°51′ N and 41°15′ N latitude.

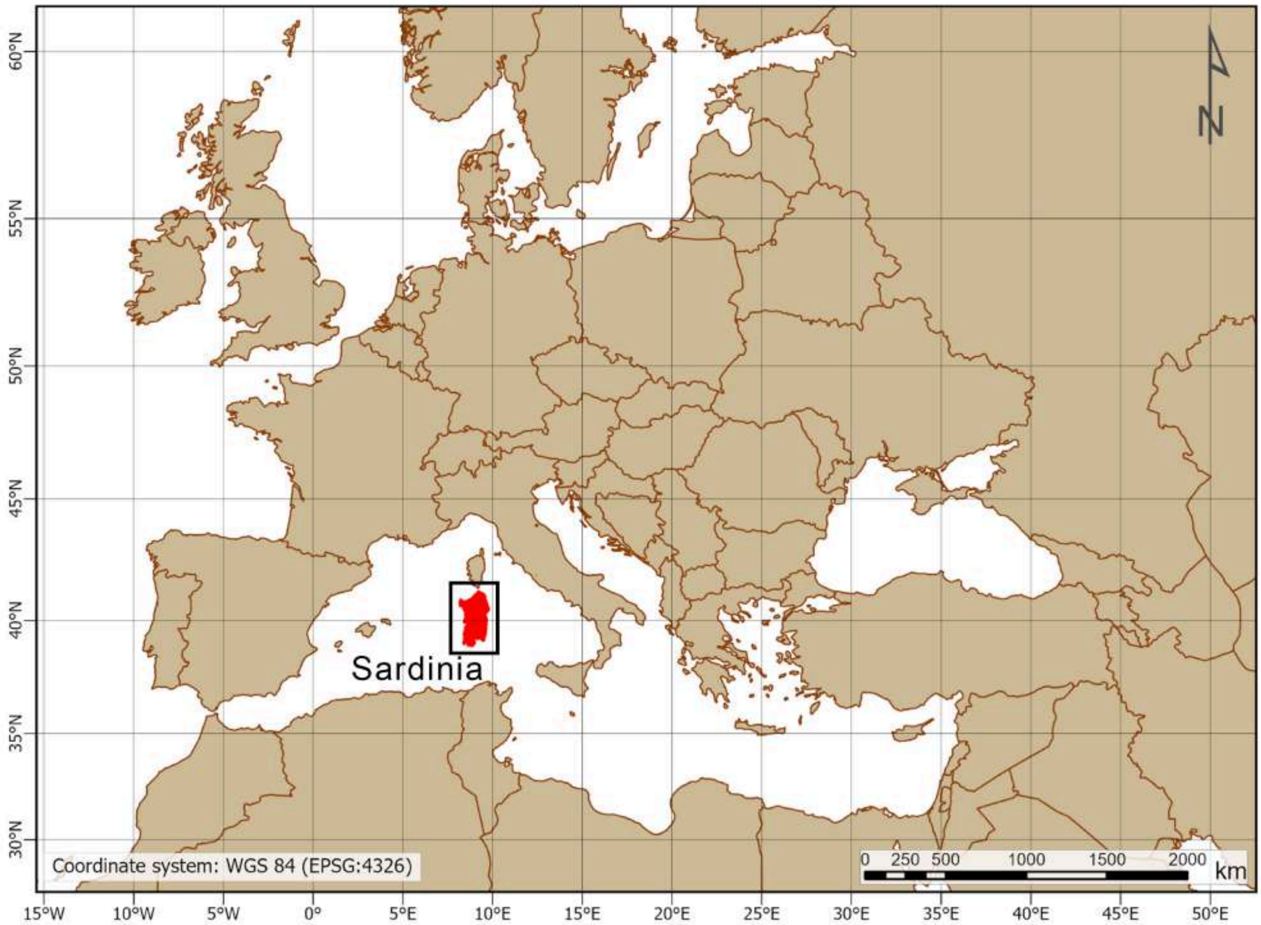

Figure 1. Location of Sardinia in the central-western Mediterranean Sea. The island, highlighted in red, is the second largest in the Mediterranean basin.

Sardinia is characterized by a highly articulated morphology (Figure 2A): plains account for roughly 18% of the territory, hill systems cover approximately 68%, and the remaining 14% is mountainous, culminating at 1834 m a.s.l. in the Gennargentu massif. The coastline extends for over 1200 km, encompassing one of the richest concentrations of coastal lagoons in the Mediterranean basin, shallow water bodies supporting a diverse mosaic of wetland habitats including saltmarshes, halophytic vegetation communities, reed beds, and transitional aquatic environments [34]. The island's environmental heterogeneity translates into a remarkably diverse habitat mosaic: according to the Carta della Natura (Figure 2B) regional survey, 93 CORINE Biotope habitat types were mapped, including extensive cork oak woodlands, holm oak forests, coastal maquis formations, and a distinctively Sardinian agro-pastoral system in which shrub understorey is systematically cleared to favour grazing beneath a sparse tree canopy [35].

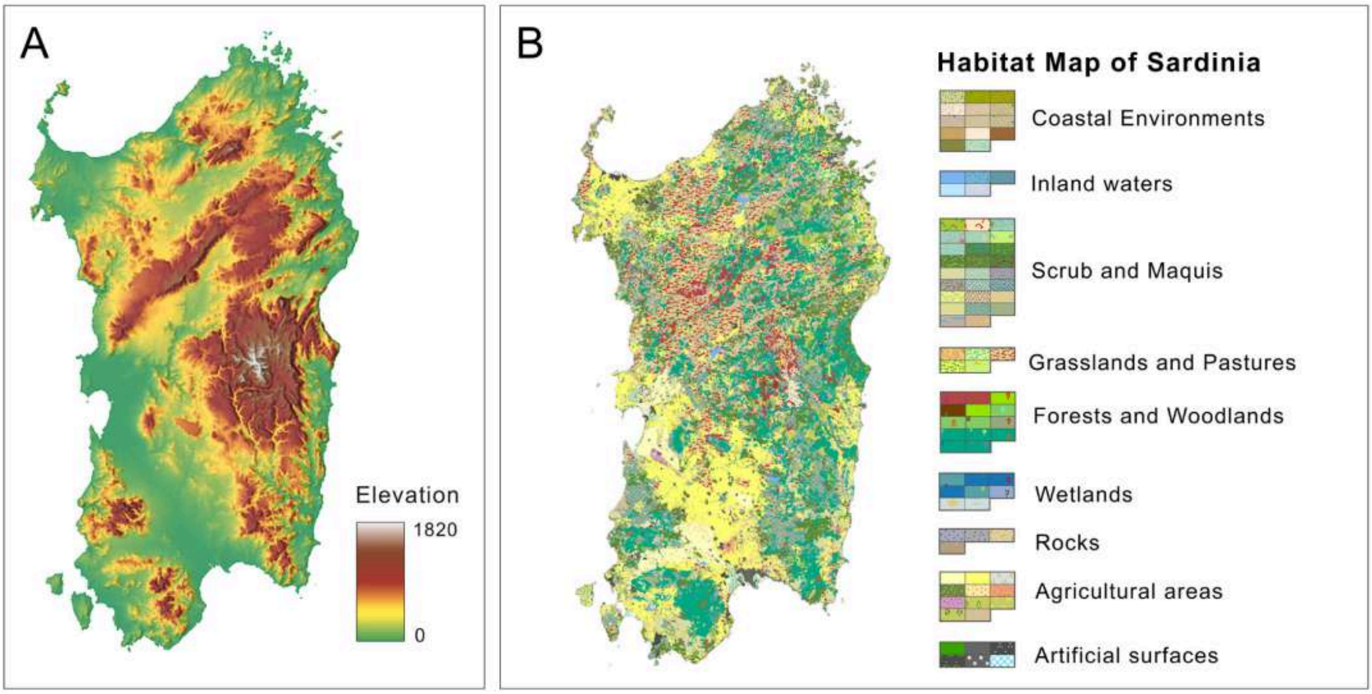

Figure 2. Overview of the main environmental characteristics of Sardinia. (**A**): Digital Terrain Model (DTM), illustrating the topographic complexity of the island, characterized by extensive upland plateau, mountain ranges in the central and eastern sectors, and low-lying coastal plains. (**B**): Habitat map of Sardinia derived from the Carta della Natura [35]. The complete legend of the habitat map is provided in the Supplementary Materials (Figure S1).

These landscape characteristics generate four specific challenges for remote sensing-based LULC classification. First, the gradual and often indistinct transitions between natural vegetation formations, particularly between dense maquis and open woodland, and between sclerophyllous shrubland and grassland, produce spectral ambiguities that are difficult to resolve at 10 m resolution. Second, wetland environments along the western and southern coasts are characterized by exceptional internal heterogeneity, with halophilous and non-halophilous vegetation communities forming spatially interlocked mosaics whose boundaries cannot be reliably detected through spectral information alone.

Third, Sardinia's strong agro-pastoral vocation [34], extensive farming systems and complex agricultural systems together with Mediterranean post-cultivation grasslands, have shaped a territory characterized by fine-grained spatial fragmentation: small, highly fragmented parcels bearing orchards, vineyards, olive groves, mixed arable crops, and kitchen gardens coexist within limited areas, frequently bounded by linear landscape elements and intermingled with progressively abandoned plots (Figure 3), generating a patchwork in which distinct land covers are often not spatially separable at the mapping scale [35,36]. Furthermore, the boundary between natural and anthropogenic land cover is often functionally and spectrally indistinct, posing significant challenges for remote sensing-based LULC classification [36].

A detailed description of the Habitat Map of Sardinia, including the complete legend and areal distribution of habitat classes derived from the Carta della Natura regional survey, is provided in the Supplementary Materials (Figures S1 and S2).

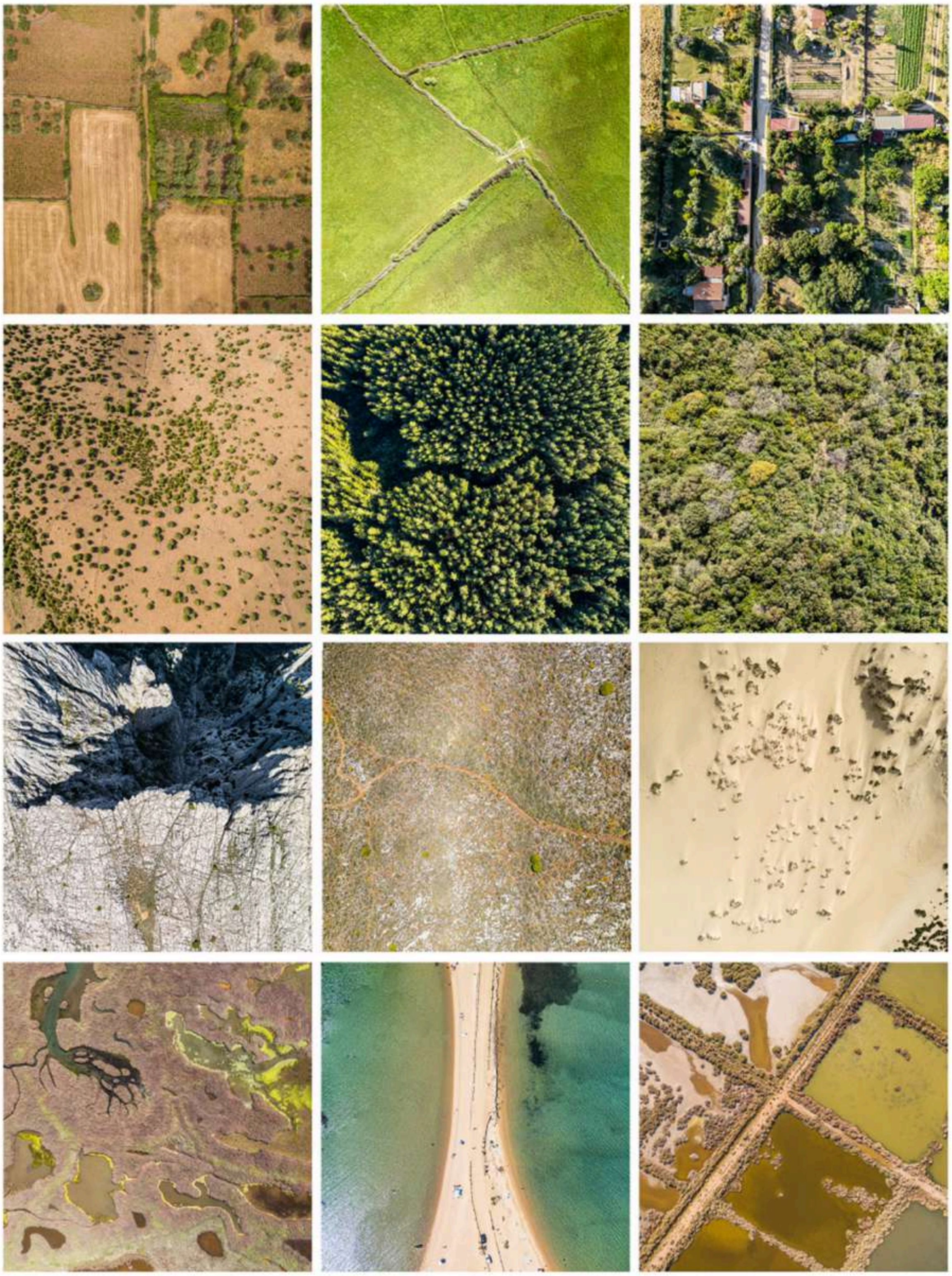

Figure 3. Representative examples of land cover types across Sardinia, captured by nadir-view drone imagery acquired during field campaigns conducted for Sardinia Land Cover Project.

3. Materials and Methods

The LULC map of Sardinia was produced for the reference year 2020, with a classification legend based on the CORINE Land Cover (CLC) hierarchy, extended to the third and selected fourth-level classes, and adapted to prioritize land cover over land use wherever spectral information allows reliable discrimination (Table 1).

Table 1. Classification legend of the Sardinia LULC map for the reference year 2020, with the corresponding CLC code, class name, and map color.

CLC Code		Class Name
	1.1.1	Built-up surfaces
	1.1.2	Other artificial surfaces
	1.2.1	Industrial or commercial areas
	1.2.2	Road and rail networks
	1.2.3	Port areas
	1.2.4	Airports and heliports
	1.3.1	Mineral extraction sites
	1.3.2	Dump sites
	1.3.3	Construction sites
	1.4.1	Urban green areas
	1.4.2	Sport and leisure facilities
	2.1.1	Non-irrigated arable land
	2.1.2.1	Irrigated arable land
	2.1.2.2	Rice fields
	2.1.2.4	Greenhouse crops
	2.2.1	Vineyards
	2.2.2	Fruit trees and berry plantations
	2.2.3	Olive groves
	2.4.2	Complex cultivation patterns
	3.1.1	Broadleaved forest
	3.1.2	Coniferous forest
	3.2.1	Natural grassland
	3.2.2	Non-sclerophyllous shrub vegetation
	3.2.3	Sclerophyllous vegetation
	3.3.1	Beaches and sandy areas
	3.3.2	Bare rock
	3.3.3	Sparsely vegetated areas
	3.3.4	Burned areas
	4.1.1	Non-halophilous marsh vegetation
	4.2.1	Halophilous marsh vegetation
	4.2.2	Salines
	5.1.1	Water courses
	5.1.2	Water bodies
	5.2.1	Coastal lagoons
	5.2.3	Sea and Ocean

The methodology (Figure 4) consists of a semi-automatic workflow combining satellite imagery, ancillary geospatial data, and iterative accuracy-driven refinement, articulated in three main components: (1) pixel-based classification, (2) image segmentation and polygon pre-labelling, and (3) reclassification and accuracy assessment. The first two components produced a preliminary map in which each polygon was assigned the dominant land cover class from the pixel-based output. This preliminary product was then refined through an iterative cycle in which accuracy assessment and reclassification were conducted concurrently: confusion matrix analysis guided the identification of systematic classification errors and problematic classes, which were addressed through a combination of semi-automatic methods, including spectral threshold rules, pixel-based classifiers, and integration of ancillary datasets, and expert photo-interpretation where errors were not amenable to automatic correction. All GIS operations, image segmentation, reclassification, and accuracy assessment were performed within the IMPACT Toolbox (European Commission Joint Research Centre, Ispra, Italy; https://forobs.jrc.ec.europa.eu/IMPACT) [37], a web-GIS platform developed by the Joint Research Centre of the European Commission and deployed on the local server of the University of Cagliari. CORINE class of burned areas is provided as a complementary thematic layer accompanying the LULC map derived from a separate study using a multi-temporal Sentinel-2 MSI approach and a Random Forest classifier specifically calibrated for the Sardinian landscape [38].

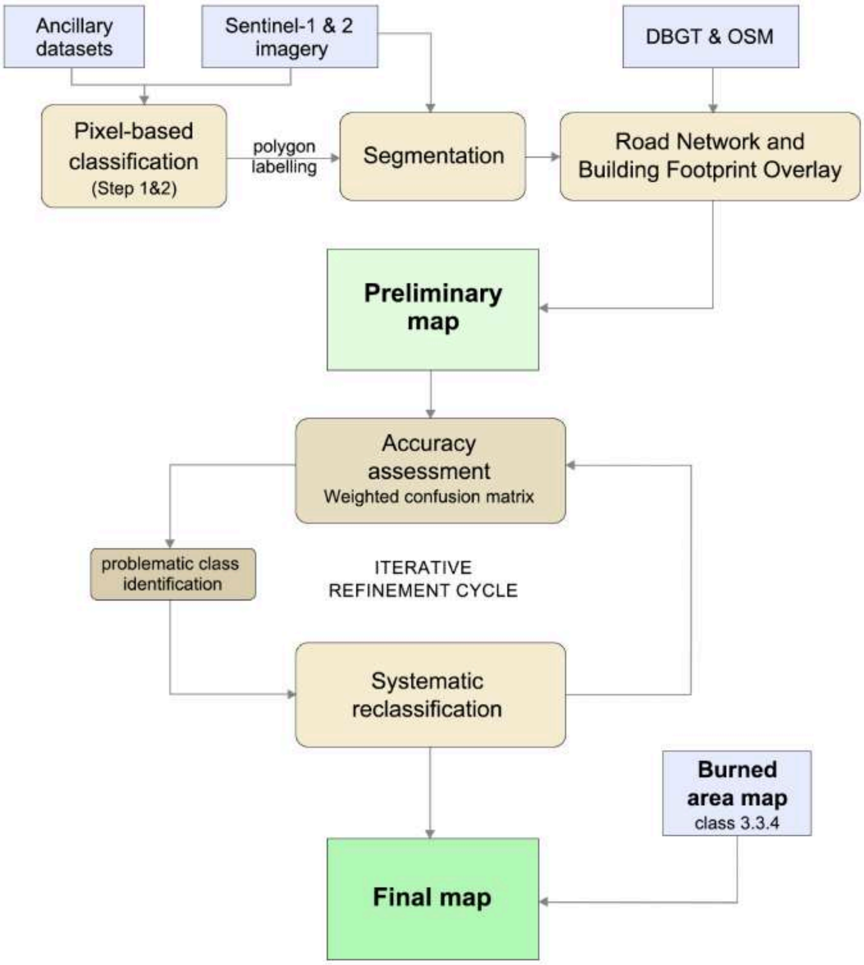

Figure 4. Overview of the semi-automatic workflow for LULC mapping of Sardinia (reference year 2020). The methodology combines pixel-based cascade classification on GEE, image segmentation and polygon pre-labelling in the IMPACT Toolbox, and an iterative accuracy-driven reclassification cycle in which confusion matrix analysis identifies systematic errors by class. Burned area polygons (CORINE class 3.3.4), derived from a separate multi-temporal Sentinel-2 and Random Forest workflow, are provided as a complementary annually updatable thematic layer.

The classification workflow relied on a combination of satellite imagery and ancillary geospatial datasets (Table 2). Satellite data included Sentinel-1 GRD (C-band SAR, VV and VH polarisations, 10 m) and Sentinel-2 Level-2A multispectral imagery (10–60 m, 13 bands), both processed on Google Earth Engine (Google LLC., Mountain View, CA, USA; https://earthengine.google.com). Ancillary vector datasets comprised the Sardinian Geo-Topographic Database (DBGT 10K, 2022), OpenStreetMap (OpenStreetMap Foundation, Cambridge, UK; https://www.openstreetmap.org), and CORINE Land Cover 2018, providing thematic information on urban fabric, transport networks, hydrography, and vegetation. From the satellite imagery, a set of spectral and temporal products was derived on GEE (Table 3), including Sentinel-1 annual and monthly composites, Sentinel-2 annual and monthly composites, multi-temporal NDVI statistics and time series, an NDFI time series for flooded surface detection, and a Phenological Based Synthesis (PBS) classification capturing vegetation and water seasonality. These products were used as input for both the pixel-based classification and the image segmentation steps.

Table 2. Input datasets used in the LULC classification workflow, including satellite imagery and ancillary geospatial data sources, with their respective roles in the classification, reclassification, and validation phases.

Dataset	Source	Description	Role in the Workflow
Sentinel-1 (Level-1 GRD)	ESA/GEE	C-band SAR imagery, VV and VH polarisations, 10 m resolution, IW mode. Acquisitions from 2019–2020. Pre-processed following [39].	Pixel-based classification; Object-based classification
Sentinel-2 (Level-2A)	ESA/GEE	Multispectral imagery, 10–60 m resolution, 13 spectral bands. Multiple cloud masking strategies applied depending on the derived product. Acquisitions from 2017–2020.	Pixel-based classification; Object-based classification; Reclassification/error correction
Geo-Topographic Database (DBGT 10K, 2022)	Sardinian Geoportal	Vector database at 1:10,000 scale. Layers used: ST01 (roads and transport), ST02 (built-up), ST04 (hydrography), ST06 (vegetation).	Pixel-based classification; Reclassification/error correction
Land Use Map (2008)	Sardinian Geoportal	Regional land use map at 1:25,000 scale, classified according to the CLC legend, produced by photointerpretation of optical imagery.	Pixel-based classification
OpenStreetMap (OSM)	Open-StreetMap	Vector dataset including buildings, roads, railways, land use, hydrography, and natural features. Downloaded December 2022.	Pixel-based classification; Reclassification/error correction
Global Human Settlement Layer (GHSL)	JRC	Global built-up presence map at 30 m resolution, derived from Landsat imagery using machine learning [40].	Pixel-based classification
CORINE Land Cover 2018 (CLC2018)	Copernicus/GEE	Pan-European land cover dataset, 100 m resolution, 44 third-level classes, MMU of 25 ha [29].	Pixel-based classification
Tree Canopy Height (TCH)	Tolan et al. [41]	Global canopy height map at 1 m resolution derived from RGB imagery using a self-supervised vision transformer and convolutional decoder trained on aerial LiDAR.	Reclassification/error correction
AGEA Orthophotos (2019, 2022)	AGEA	High-resolution aerial orthophotos at 0.20 m/pixel, 4 bands (Blue, Green, Red, NIR).	Reclassification/error correction; Validation/photo-interpretation

Table 3. Satellite-derived products generated from Sentinel-1 and Sentinel-2 imagery on the Google Earth Engine cloud computing platform, used as input for the pixel-based classification and image segmentation steps.

Product	Sensor	Description
Annual composite 2020	Sentinel-1	Annual composite of VV and VH backscatter bands at 10 m resolution, reference year 2020, produced computing the mean value per polarization over all available acquisitions of 2020, after pre-processing following [39].
Monthly composites 2020	Sentinel-1	Twelve monthly composites of VV and VH backscatter bands at 10 m resolution for the year 2020, produced computing the mean value per polarization for each calendar month over pre-processed acquisitions [39].
Biannual composite 2019–2020	Sentinel-1	Two-year composite of VV and VH backscatter bands at 10 m resolution covering 2019–2020, produced computing the mean value per polarization over all pre-processed acquisitions from 2019 and 2020 following [39].

Table 3. *Cont.*

Product	Sensor	Description
Annual composite 2020	Sentinel-2	Annual composite of all spectral bands at 10–60 m resolution, reference year 2020, produced computing the median value per band computed from cloud- and shadow-free Level-2A imagery acquired in 2020, masked following [42].
Monthly composites 2020	Sentinel-2	Twelve monthly composites of all spectral bands at 10–60 m resolution for the year 2020, produced computing the median value per band for each calendar month. Two cloud masking strategies applied: QA60 quality band for summer months; Sentinel Hub Cloud Probability layer (threshold: 30%) for remaining months, with residual gaps filled using the QA60-masked product.
Maximum NDVI map (2017–2020)	Sentinel-2	Greenest pixel composite representing the maximum NDVI value recorded at each pixel over the 2017–2020 period. Maximum NDVI value has been extracted pixel-wise from all cloud-masked Level-2A acquisitions between 2017 and 2020, following the cloud masking algorithm of [42].
Minimum NDVI map (2019–2020)	Sentinel-2	Map of the minimum NDVI value recorded at each pixel over the 2019–2020 period. Minimum NDVI value has been extracted pixel-wise from cloud-masked Level-2A acquisitions from 2019 and 2020, following [42].
NDVI statistics map (2020)	Sentinel-2	Per-pixel statistical summary of the NDVI time series for 2020, including minimum, maximum, median, and standard deviation. Statistical metrics were computed pixel-wise from the monthly NDVI time series derived from Sentinel-2 monthly composites of 2020.
NDVI time series (2020)	Sentinel-2	Dense NDVI time series at pixel level for the growing season (April–October 2020), used to characterize crop phenology. NDVI was computed from all available cloud-masked Level-2A acquisitions between 1 April 2020 and 31 October 2020. The resulting time series was smoothed using a linear regression algorithm with a 22-day moving window to reduce residual cloud noise.
NDFI time series (2020)	Sentinel-2	Dense NDFI time series at pixel level for the growing season (April–October 2020), used to detect soil flooding associated with rice cultivation. NDFI was computed from all available cloud-masked Level-2A acquisitions between 1 April 2020 and 31 October 2020. No smoothing applied to preserve isolated flooding signals.
Phenological Based Synthesis (PBS) classification (2019–2020)	Sentinel-2	Thematic land cover classification based on vegetation and water seasonality, providing per-pixel phenological classes. PBS algorithm [43], adapted for Sentinel-2 using the cloud masking procedure of [42], applied to all available acquisitions from 2019 and 2020 (295 images total).
Annual composite 2020 (S1 and S2 combined)	Sentinel-1 Sentinel-2	Three-band composite combining Sentinel-2 GREEN and NIR bands with the mean of Sentinel-1 VV and VH polarization, used as input for image segmentation. Sentinel-2 GREEN (B3) and NIR (B8) bands were extracted from the Sentinel-2 surface reflectance annual composite 2020; the mean of VV and VH backscatter was extracted from the Sentinel-1 annual composite 2020. The three bands were stacked into a single multi-band image. Prior to segmentation, all bands were linearly rescaled to an 8-bit range (0–255) in order to reduce computational complexity and improve processing efficiency within the Baatz multiresolution segmentation workflow implemented in IMPACT Toolbox. Since the segmentation algorithm primarily relies on relative spectral heterogeneity between neighboring pixels, the reduced radiometric depth was considered sufficient for object delineation purposes.

3.1. Pixel-Based Classification

Pixel-based classification was performed on the GEE platform following a cascade classifier system articulated in two sequential steps. In the first step (Step 1), land cover information was initialised from multiple ancillary datasets through a sequential assignment logic in which an initially empty classification layer is progressively populated using conditional rules applied in a predefined order. This ordering explicitly encodes the relative confidence and thematic reliability of each data source. The classification relies on three main categories of rules: (i) gap-filling rules, which assign class labels exclusively to previously unclassified pixels; (ii) priority-based overwriting rules, where high-confidence datasets systematically replace existing labels regardless of prior assignments; and (iii) condition-driven rules, which combine ancillary layers with spectral and SAR-derived metrics to resolve ambiguous or transitional land cover conditions. The hierarchical priority scheme reflects geometric accuracy, thematic reliability, and temporal proximity of each source to the 2020 reference year. DBGT and OSM are assigned the highest priority: DBGT as the official regional geo-topographic database, and OSM for its comparable completeness and geometric accuracy for infrastructure classes not fully covered by DBGT. The 2008 Land Use Map is assigned to intermediate priority, providing reliable thematic guidance for temporally stable classes but treated with lower confidence for dynamic classes given its twelve-year temporal gap. CLC2018 is restricted to gap-filling due to its coarse spatial resolution and large MMU, incompatible with the geometric requirements of the present map. Global products such as GHSL are used conservatively as a last resort to reduce unclassified areas. Post-assignment correction rules are finally implemented to identify and recode systematic inconsistencies between ancillary data and satellite-derived indicators, using threshold-based conditions on spectral indices and SAR backscatter. Spectral and SAR-based thresholds applied in the post-assignment correction rules were defined through two complementary approaches. Where established values exist in the literature, such as NDVI thresholds for vegetation discrimination, these were used as a reference, deliberately adopting conservative bounds to ensure complete capture of the target class and minimizing omission errors. For PBS-based thresholds, values were derived directly from the PBS classification legend [43], which associates specific score ranges with discrete land cover and phenological classes. A detailed explanation of the cascade system and error corrections of Step 1 is shown in Figure 5.

In the second step (Step 2), agricultural pixels identified in Step 1 were processed through a further cascade of classifiers to assign sub-class labels. As in Step 1, the classification follows a sequential logic in which each classifier operates on pixels not yet assigned by the preceding one (Figure 6). Classification criteria rely on spectral indices and parameters extracted from multi-temporal analysis of Sentinel-1- and Sentinel-2-derived products, whose specific threshold values were defined through a combination of prior knowledge of the phenological cycles and spectral characteristics of the main crop types cultivated in Sardinia, local agronomic expertise, and empirical trial-and-error optimization. Where established phenological or spectral thresholds were available from the literature, these were used as initial reference values and subsequently refined iteratively to maximize class separability and classification accuracy over the study area.

Classification criteria in Step 2 relied on a set of spectral indices and parameters derived from Sentinel-1 and Sentinel-2 time series (Table 4), including NDVI-based statistics (median, minimum, maximum, amplitude, and timing of seasonal extremes), SAR backscatter metrics, visible band brightness ratios, and flood-sensitive indices. These features were selected to capture the key spectral and phenological characteristics that differentiate crop types and other land cover classes within the agricultural mask under Mediterranean conditions.

The approach combines four main strategies: (i) direct import from ancillary datasets for classes assumed to be spatially stable, such as permanent crops from DBGT; (ii) threshold-based rules on NDVI statistics and SAR backscatter for spectrally distinct surfaces such as water bodies, wetlands, greenhouse crops, and tree cover; (iii) phenology-driven classifiers exploiting the temporal shape of the NDVI and NDFI time series to discriminate crop types with characteristic seasonal cycles, including vineyards, irrigated arable lands, and rice fields; and (iv) a residual gap-filling step assigning non-irrigated arable land to all unclassified agricultural pixels. The full set of spectral thresholds and classification criteria for each class is reported in Table 5.

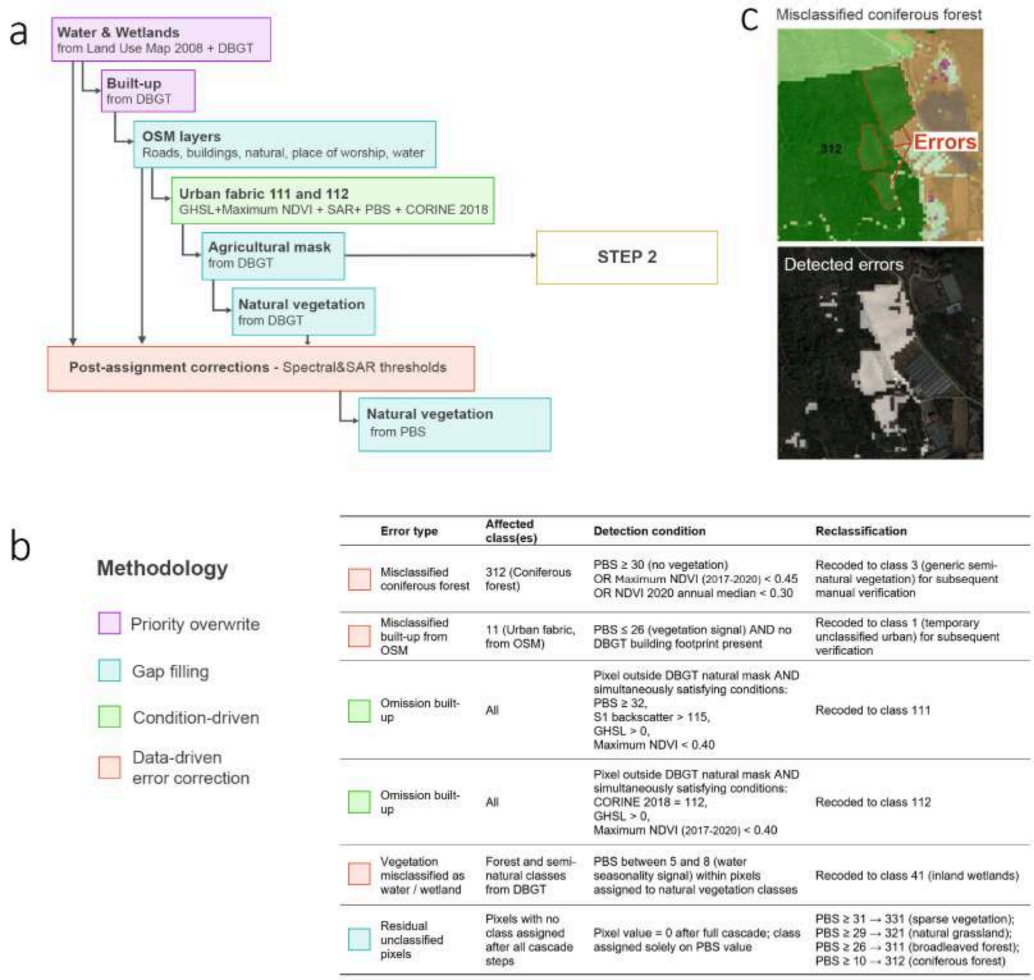

Error type	Affected class(es)	Detection condition	Reclassification
Misclassified coniferous forest	312 (Coniferous forest)	PBS ≥ 30 (no vegetation) OR Maximum NDVI (2017-2020) < 0.45 OR NDVI 2020 annual median < 0.30	Recoded to class 3 (generic semi-natural vegetation) for subsequent manual verification
Misclassified built-up from OSM	11 (Urban fabric, from OSM)	PBS ≤ 26 (vegetation signal) AND no DBGT building footprint present	Recoded to class 1 (temporary unclassified urban) for subsequent verification
Omission built-up	All	Pixel outside DBGT natural mask AND simultaneously satisfying conditions: PBS ≥ 32, S1 backscatter > 115, GHSL > 0, Maximum NDVI < 0.40	Recoded to class 111
Omission built-up	All	Pixel outside DBGT natural mask AND simultaneously satisfying conditions: CORINE 2018 = 112, GHSL > 0, Maximum NDVI (2017-2020) < 0.40	Recoded to class 112
Vegetation misclassified as water / wetland	Forest and semi-natural classes from DBGT	PBS between 5 and 8 (water seasonality signal) within pixels assigned to natural vegetation classes	Recoded to class 41 (inland wetlands)
Residual unclassified pixels	Pixels with no class assigned after all cascade steps	Pixel value = 0 after full cascade; class assigned solely on PBS value	PBS ≥ 31 → 331 (sparse vegetation); PBS ≥ 29 → 321 (natural grassland); PBS ≥ 26 → 311 (broadleaved forest); PBS ≥ 10 → 312 (coniferous forest)

Figure 5. Overview of the Step 1 pixel-based classification workflow: (**a**) schematic diagram of the cascade classifier system, in which each node represents a classification step colour-coded by rule type: priority overwrite (purple), gap filling (blue), condition-driven assignment (green), and data-driven error correction (salmon); (**b**) summary table of post-assignment correction rules applied within Step 1, reporting for each error type the affected classes, the detection conditions, and the resulting reclassification; (**c**) example of misclassified coniferous forest (class 3.1.2) detected through spectral consistency analysis, showing the flagged polygons (red outlines) overlaid on a Sentinel-2 composite (**top**) and the corresponding pixel-level error detection output (**bottom**).

Table 4. Spectral indices and parameters extracted from Sentinel-1 and Sentinel-2 satellite products and used as classification criteria in Step 2 of the pixel-based classification workflow. For each index or parameter, the formula and a brief description of its thematic sensitivity are reported.

Spectral Index or Parameter	Formula	Description
VV_{min}	-	Minimum value of VV time series of Sentinel-1 monthly composites.
NDVI	$\frac{NIR - RED}{NIR + RED}$	Normalized Difference Vegetation Index, measures density and health of vegetation. Sentinel-2 B8 and B4 bands have been used.
$NDVI_{median}$	-	Median value of NDVI time series of Sentinel-2 monthly composites.

Table 4. *Cont.*

Spectral Index or Parameter	Formula	Description
$NDVI_{max}$	-	Maximum value of NDVI time series of Sentinel-2 monthly composites.
$NDVI_{min}$	-	Minimum value of NDVI time series of Sentinel-2 monthly composites.
$Time_{max}$	-	Time when the maximum value of NDVI was found. $Time_{max}$ is expressed in month number (1–12) for the NDVI time series of monthly composites, and in Day of the Year (DoY) for the detailed NDVI time series.
$Time_{min}$	-	Time, expressed in month number (1–12), when the minimum value of NDVI was found.
Amplitude	$NDVI_{max} - NDVI_{min}$	Difference between maximum and minimum values of NDVI.
RB	$\frac{RED}{RED + GREEN + BLUE} \times 100$	Red brightness percentage in VIS spectral range. Sentinel-2 B4, B3 and B2 bands have been used.
GB	$\frac{GREEN}{RED + GREEN + BLUE} \times 100$	Green brightness percentage in VIS spectral range. Sentinel-2 B4, B3 and B2 bands have been used.
BB	$\frac{BLUE}{RED + GREEN + BLUE} \times 100$	Blue brightness percentage in VIS spectral range. Sentinel-2 B4, B3 and B2 bands have been used.
NDSI	$\frac{SWIR_1 - NIR}{SWIR_1 + NIR}$	Normalized Difference Soil Index, sensitive to bare soils and artificial surfaces. Sentinel-2 B11 and B8 bands have been used.
NGRDI	$\frac{GREEN - RED}{GREEN + RED}$	Normalized Green–Red Difference Index, sensitive to vegetation density. Sentinel-2 B3 and B4 bands have been used.
NDFI	$\frac{RED - SWIR_1}{RED + SWIR_1}$	Normalized Difference Flood Index, sensitive to soil submergence typical of flooded rice fields. Sentinel-2 B4 and B11 bands have been used.

Table 5. Classification criteria applied in Step 2 of the pixel-based classification workflow for each land cover class within the agricultural mask. For each class, the table reports the spectral indices, parameter thresholds, and phenological conditions used for class assignment, along with a brief description of the classification approach and the spectral or phenological basis for the selected criteria.

Class	Criteria or Spectral Indices/Parameter Threshold	Description
Permanent crops	Imported from DBGT	Permanent crops were imported directly from the DBGT, under the assumption of inter-annual stability for these land cover types. An additional classification step was applied for vineyards (see below) to recover omission errors not covered by the ancillary dataset.
Water bodies	$NDVI_{median} < 0$	Water bodies and wetlands misclassified as agricultural areas in Step 1 were identified using negative or very low NDVI values. While water bodies are characterized by consistently negative NDVI, wetlands may exhibit slightly higher values due to the presence of emergent or fringe vegetation, making NDVI alone insufficient for their discrimination from bare soils. The minimum VV backscatter threshold ($VV_{min} < -19$ dB) was therefore applied as an additional criterion: open and shallow water surfaces—including seasonally flooded areas typical of Mediterranean wetlands—produce very low SAR backscatter due to specular reflection, whereas bare soils return higher backscatter values regardless of their moisture content.
Wetlands	$NDVI_{min} < 0.10$ $VV_{min} < -19$	
Greenhouse crops	$0 < NDVI_{median} < 0.35$ $NDVI_{max} < 0.55$ $NDVI_{min} < 0.15$ $VV_{min} < -18$ $\rho BLUE_{August} > 1000$ $12\% < (RB - BB)_{Aug} < 20\%$	Greenhouse crops are characterized by dark or very bright surfaces, with a higher reflectance in blue spectral range than natural surfaces (vegetation, soils, etc.). For these reasons, low values of NDVI, minimum VV polarization and spectral characteristics in blue and red spectral ranges were selected to detect this type of land cover.
Bare soils	$0 < NDVI_{median} < 0.10$	Surfaces showing persistently low but non-zero photosynthetic activity throughout the year, not attributable to water bodies, wetlands, or greenhouse crops. These surfaces are incompatible with any agricultural land cover class and were flagged for subsequent reclassification.

Table 5. *Cont.*

Class	Criteria or Spectral Indices/Parameter Threshold	Description
Tree cover	$NDVI_{min} > 0.20$ Amplitude < 0.42 $\rho NIR_{August} < 3400$ $NDSI_{August} < 0.10$ $NGRDI_{August} < 0.15$ $VV\text{-}VH_{mean}$ (2019–2020) > −15 PBS < 30	Tree cover encompasses surfaces with a stable year-round NDVI signal typical of arboreal vegetation, including permanent crops (olive groves, orchards) not captured by the DBGT and trees in agroforestry. August was specifically selected for the extraction of spectral indices because, under the Mediterranean climate, herbaceous vegetation and rainfed crops are largely senescent at this time of year, maximizing the spectral contrast between arboreal and non-arboreal surfaces. The low NIR reflectance in August reflects canopy shadow effects [44]. NDSI was used to exclude residual bare soil and artificial surfaces, NGRDI to separate arboreal from herbaceous vegetation, and SAR VV-VH backscatter to identify structurally complex surfaces. The PBS threshold excludes pixels with no vegetation signal across the year. Given the spectral similarity among different arboreal types, this class was assigned a temporary generic code for subsequent refinement.
Vineyards	$NDVI_{Apr} < NDVI_{May} < NDVI_{Jun}$ $NDVI_{Nov} < NDVI_{Oct}$ $NDVI_{Aug} < 0.50$ $NDVI_{max} < 0.80$ $NDVI_{min} > 0.10$ $\rho NIRNDVI_{max} > 4100$	Vineyard classification was based on vine phenological cycle, characterized by a growing season in spring and summer and a dormancy in autumn and winter. NDVI time series was used for the recognition of these phenological stages. In addition, it was observed that the NIR reflectance of vineyards registered in the month in which the highest photosynthetic activity is recorded ($NDVI_{max}$) is always lower compared to arable lands, thus this characteristic was used for better discrimination between these two types of crops.
Irrigated arable lands	C1: ΔNDVI (max − min) > 0.40 in July and/or August C2: Positive NDVI slope from 1 June to 15 August, with ΔNDVI > 0.20 C3: Positive NDVI slope from 21 May to 30 June, with ΔNDVI > 0.20 C4: Positive NDVI slope from 1 July to 31 August, with ΔNDVI > 0.30 C5: Positive NDVI slope from 1 August to 21 August, with ΔNDVI > 0.20 C6: max NDVI (June) > 0.60 AND $maxNDVI_{June} - maxNDVI_{April\text{–}May} > 0.30$ C7: Mean NDVI from 1 June to 31 August > 0.60 AND σ < 0.06 A pixel is classified as irrigated if it satisfies at least one criterion.	Irrigated arable lands were identified based on NDVI temporal dynamics indicative of summer crop growth. In Mediterranean environments, rainfed vegetation typically senesces during early summer, whereas irrigated crops maintain or increase greenness due to external water supply. This approach represents a simplification, as it effectively identifies only summer-irrigated crops, potentially missing irrigated surfaces with different seasonal calendars. However, this approximation is necessary given the high variability of crop types and agricultural practices across the Sardinian territory, which prevents a more precise characterization of irrigation at this scale. Criteria target different aspects of summer vegetative dynamics: intra-monthly NDVI variability (C1), positive NDVI slope across different sub-seasonal windows (C2–C5), rapid early-summer NDVI increase (C6), and high stable summer NDVI indicative of continuous irrigation (C7). The amplitude threshold ensures the detection of significant vegetation growth and reduces noise-related effects, while multiple temporal conditions capture variability in crop calendars and growth dynamics, allowing detection of both early and late NDVI increases and reducing omission errors linked to rigid phenological assumptions. A 15 m focal minimum spatial filter was applied to improve spatial coherence and reduce pixel-level noise.
Rice fields	$NDVI_{max} > 0.40$ $150 < Time_{max} < 250$ (DoY) $NDFI_{flood} > 0$ $Timeflood < Time_{max}$ $Probability_{flood} < 10\%$ $CP_{flood} < 80\%$ $Time_{flood1} \neq Time_{flood2}$	Rice cultivation in Sardinia may involve the distinctive practice of flooding of the fields (usually during spring) before the establishment of the crop and successive rapid growth of rice plants, with the maximum photosynthetic activity reached in summer and maturation in October, before the harvest. The detection of rice fields from satellite data is usually achieved through the recognition of the flooding signal [45]. This signal can be identified by positive values of the NDFI index, registered before the growth of rice plants [46]. For rice field classification, the detailed NDVI and NDFI time series were used to detect the flooding condition and phenological stages of rice. However, residual cloud contamination may cause positive values of NDFI. To reduce this issue, pixels presenting isolated positive values of NDFI occurring with a cloud probability higher than 10% and a cloudy pixel percentage (CP) of the source image higher than 80% were excluded.
Non-irrigated arable lands	All the pixel not classified in previous steps	All agricultural pixels not assigned to any of the above classes were automatically classified as non-irrigated arable lands, on the assumption that the absence of a summer NDVI peak indicates reliance on rainfall rather than artificial irrigation.

The ordering of classifiers reflects the spectral and phenological separability of each class: ancillary-derived classes are assigned first, followed by spectrally unambiguous surfaces, phenologically characterized crop types, and finally non-irrigated arable land as a residual gap-filling class.

In addition to the crop-specific classifiers, dedicated correction classifiers were implemented to identify and recode surfaces erroneously included within the agricultural mask during Step 1, as well as to recover omission errors from previous classification steps. These include tree cover elements, encompassing both agroforestry features and permanent crops such as olive groves and orchards not captured by the DBGT; wetlands; and bare or persistently unvegetated surfaces whose spectral signatures are incompatible with any agricultural land cover class. The identification of these surfaces relied on a combination of spectral indices, SAR backscatter metrics, and PBS-derived phenological information. Given the spectral similarity among several of these categories, surfaces that could not be unambiguously assigned to a specific CORINE class were labelled with generic temporary codes for subsequent refinement during the reclassification phase.

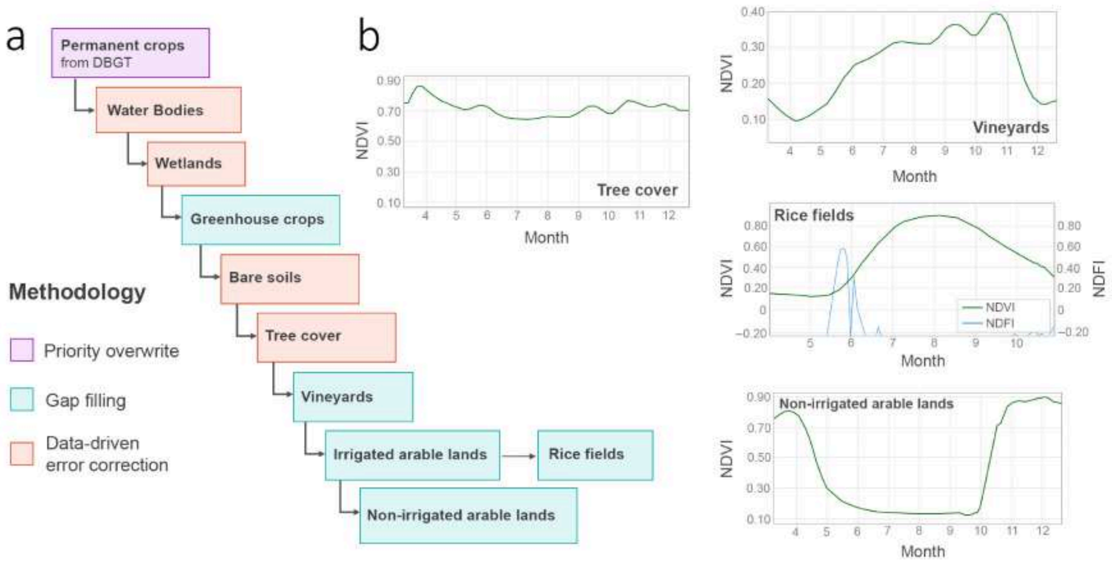

Figure 6. Overview of the Step 2 pixel-based classification workflow: (**a**) schematic diagram of the cascade classifier system for agricultural and mixed land cover classes, colour-coded by rule type; (**b**) representative NDVI temporal profiles extracted from Sentinel-2 time series illustrating the phenological basis of the classification criteria adopted in Step 2, for selected classes: tree cover (stable year-round signal), vineyards (spring growth and autumn senescence), rice fields (early-season flooding signal in NDFI followed by rapid summer NDVI peak [45,46]), and non-irrigated arable lands (winter–spring growth and summer senescence).

3.2. Image Segmentation and Polygon Pre-Labelling

Image segmentation was performed within the IMPACT Toolbox [37,47], first deployed for Sardinia land cover mapping in [47], extending that preliminary contribution through a complete 35-class legend, iterative accuracy-driven reclassification, and full regional validation. Segmentation followed the multi-resolution algorithm of Baatz and Schäpe [48,49], applied to a three-band input image composed of the Sentinel-2 annual composite GREEN and NIR bands (B3 and B8) and the mean of Sentinel-1 VV and VH annual composite bands. The selection of these bands reflects complementary information content: the Sentinel-2 GREEN and NIR bands provide high spectral separability for vegetation types, while the Sentinel-1 VV-VH mean captures the structural characteristics of the land surface, improving the delineation of boundaries between spectrally similar but structurally distinct classes. The segmentation parameters were determined through iterative trial-and-error optimization on representative sample areas covering the main land cover types present in the study area. Parameter selection was guided by two complementary criteria: the visual quality of the resulting segmentation, assessed in terms of boundary delineation accuracy and intra-segment homogeneity, and the total number of output polygons, seeking a compromise between segmentation detail and computational manageability of the resulting vector file. The final parameter combination was as follows: MMU = 4 pixels/400 m^2, color = 0.9, compactness = 0.7, and similarity = 0.82. Each polygon was subsequently labelled with the land cover class derived from the pixel-based classification most frequently occurring within its boundary, applying a majority rule threshold of 50%. An exception was made for irrigated arable lands, for which a lower threshold of 30% was adopted; thus, a polygon was classified as irrigated if at least 30% of its constituent pixels were assigned to that class by the pixel-based classifier. This threshold was determined through visual cartographic assessment: at the standard 50% majority threshold, irrigated polygons were systematically underrepresented in the preliminary map because their constituent pixels frequently did not reach the majority threshold due to the fine-grained spatial heterogeneity of irrigated parcels in Sardinia. The threshold was progressively reduced from 50% until polygon assignments achieved cartographic consistency with observed field patterns. Post hoc analysis confirmed that the 30% threshold also maximizes the F1 score for the irrigated arable class (F1 = 82.65%), representing the optimal balance between User Accuracy (88.4%) and Producer Accuracy (77.6%) across the tested range (10–60%, Figure 7). Notably, the F1 difference between the 30% and the standard 50% threshold is only 3 percentage points (82.65% vs. 79.67%), confirming that this choice did not substantially inflate the accuracy of the class.

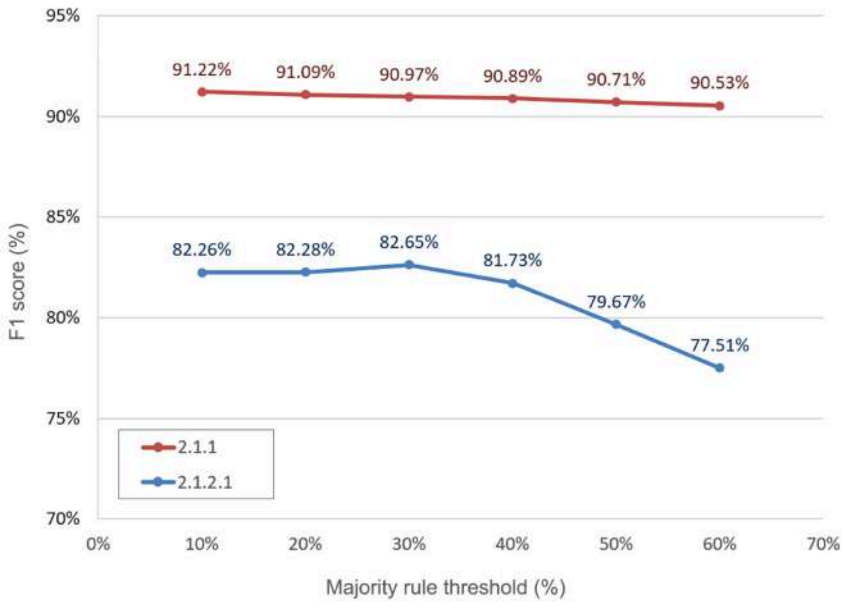

Figure 7. F1 score for irrigated arable land (2.1.2.1) and non-irrigated arable land (2.1.1) as a function of the majority-rule threshold applied during polygon pre-labelling (range: 10–60%). The F1 score is computed as the harmonic mean of User Accuracy and Producer Accuracy. The selected threshold of 30% maximizes the F1 score for the irrigated arable class (F1 = 82.65%), while the non-irrigated class remains stable across all tested values (~98.7–98.8%).

3.3. Road Network and Building Footprint Overlay

Following segmentation and polygon pre-labelling, road networks, railways, and building footprints derived from OSM and DBGT were geometrically overlaid onto the segmented vector map through an Erase and Union procedure. This operation was performed after segmentation rather than as a pre-processing step, because the spatial resolution of Sentinel imagery (10 m) is insufficient to delineate linear infrastructure features such as roads and individual buildings, which would therefore not generate meaningful segments if included in the segmentation input. By overlaying these vector layers after segmentation, their native geometric precision is preserved and incorporated into the final map without interfering with the spectral homogeneity criteria used during segmentation.

3.4. Reclassification and Accuracy Assessment

Reclassification and accuracy assessment were conducted as concurrent and mutually informing activities throughout the production of the map. Confusion matrix analysis, computed at both the second and third/fourth CLC levels using a weighted validation dataset, was used to systematically identify classes with insufficient producer or user accuracy, diagnose the sources of confusion, and prioritize targeted reclassification interventions.

It is important to clarify the nature of the interaction between accuracy assessment and reclassification within this iterative cycle. At no stage were individual control points examined: the confusion matrix was used exclusively at the class level to identify which classes presented insufficient accuracy and to diagnose the nature of the confusion, whether attributable to spectral ambiguity, ancillary data inconsistency, or structural landscape complexity. This class-level diagnostic information determined the type of correction strategy to be applied: semi-automatic spectral reclassification, integration of new ancillary datasets, or systematic manual photointerpretation. Corrections were always applied uniformly to all polygons across the entire study area, irrespective of whether those polygons contained validation points. The reference dataset therefore remained spatially blind to all reclassification decisions throughout the production process. Similarly, the spectral and structural thresholds applied throughout the reclassification workflow were defined based on literature values, PBS classification legend specifications, and local agronomic and ecological expertise, not derived by optimizing accuracy metrics against the reference dataset. The confusion matrix informed which classes required intervention and what type of correction was appropriate, but the specific parameter values governing each correction were determined independently of the validation data. The robustness of the accuracy estimate is further supported by the statistical properties of the reference dataset: 11,575 control points distributed through stratified random sampling across the entire study area (average density ~1 point per 2 km^2) constitute a representative sample of the full polygon population. At this density, class-level accuracy metrics are stable estimators insensitive to corrections applied to individual polygons, and the probability that reclassification operations systematically co-occurred with validation point locations, rather than affecting the broader polygon population uniformly, is negligible. The iterative use of class-level confusion matrices to guide reclassification is methodologically analogous to cross-validation diagnostics in supervised classification, where aggregate error statistics inform model refinement without compromising the independence of the final evaluation.

3.4.1. Reclassification

Reclassification operations were carried out through three complementary approaches: semi-automatic threshold-based reclassification and manual photointerpretation. These methods were applied selectively depending on the nature of the classification errors identified.

The introduction of high-resolution building footprint datasets from OSM and DBGT allowed the delineation of individual buildings at their native geometric resolution, making the original CORINE distinction between continuous and discontinuous urban fabric no longer applicable at the map's scale. As a consequence, the urban fabric classes were restructured: class 1.1.1, renamed "Built-up surfaces", was redefined to contain exclusively individual building footprints derived from the ancillary datasets. Class 1.1.2, renamed

"Other artificial surfaces", was defined to encompass all remaining artificial surfaces not corresponding to buildings or infrastructure, such as parking areas, paved courtyards, and other impervious surfaces. Vegetated areas previously grouped within the discontinuous urban fabric class were extracted and recoded to urban green areas (1.4.1) using PBS values between 9 and 30, corresponding to evergreen and seasonal vegetation phenological classes in the PBS legend as well as manual refinement.

Systematic spectral inconsistencies in natural vegetation classes were addressed through a combination of spectral and structural metrics. For each polygon belonging to forest and semi-natural classes, including generic semi-natural (3), generic forest (3.1), broadleaved forest (3.1.1), sparse vegetation (3.3.3), and the temporary tree cover class, the mean values of the Sentinel-2 GREEN and NIR bands and the Sentinel-1 mean VV-VH backscatter were extracted and compared against class-specific spectral thresholds and the PBS classification. The results shown in Figure 8 demonstrate clear spectral coherence, and therefore separability, among PBS classes, whereas this pattern is not observed when polygons are grouped according to CORINE classes. In particular, the distribution of the mean GREEN, NIR, and VV–VH values highlights the presence of spectrally heterogeneous objects within the same CORINE class, which can instead be discriminated through the combined use of spectral bands and PBS information.

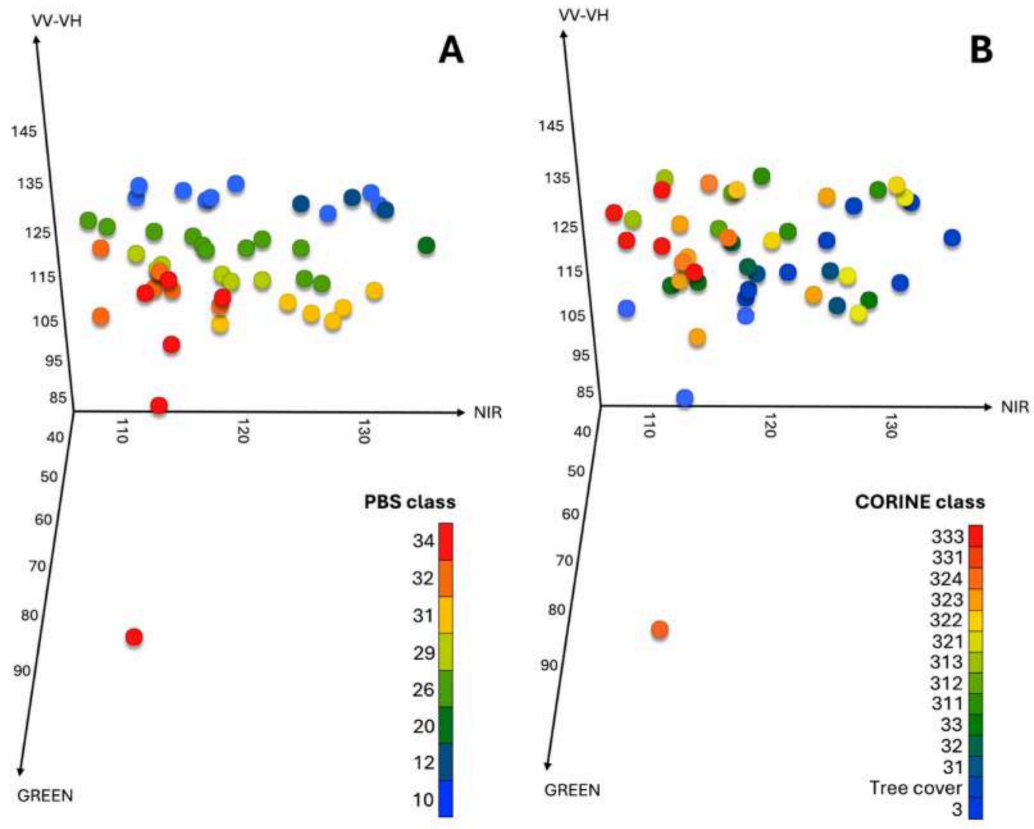

Figure 8. Three-dimensional scatter plots of polygon mean spectral values: Sentinel-2 GREEN and NIR bands and Sentinel-1 mean VV-VH backscatter, extracted from polygons belonging to forest, semi-natural, and temporary tree cover classes. (**A**): polygons colored by PBS class, showing clear spectral coherence and separability among phenological categories. (**B**): the same polygons colored by assigned CORINE class, revealing the presence of spectrally heterogeneous objects within individual CORINE classes that cannot be discriminated on the basis of thematic label alone.

Polygons whose spectral response was incompatible with their assigned class were automatically flagged and recoded into the most appropriate natural vegetation class based on threshold-based rules, empirically defined through an iterative trial-and-error procedure. In particular, flagged polygons showing PBS classes consistent with dense forest cover (PBS 10, 11, or 12) and Sentinel-1 VV-VH backscatter exceeding 125 (8-bit rescaled values), indicative of a vertically structured and rough surface, were recoded to broadleaved forest (3.1.1), while flagged polygons associated with PBS = 30 (herbaceous vegetation) and VV-VH backscatter below 125 were reassigned to natural grassland (3.2.1). The TCH dataset [41], which became available only after the initial classification processing, was subsequently integrated as a complementary structural data source to further refine the assignment of natural vegetation classes where spectral metrics alone had proven insufficient. For each polygon in classes 3.1.1, 3.2.3, 3.2.1, 3.3.3, and the temporary tree cover class, the mean TCH value was computed and compared against class-specific canopy height thresholds: polygons with mean TCH > 6 m were assigned to broadleaved forest (3.1.1), while polygons with mean TCH between 3 and 6 m were recoded to sclerophyllous vegetation (3.2.3).

The TCH dataset was used to systematically refine the assignment of natural vegetation classes by applying a consistent set of canopy height thresholds across multiple classes: polygons with mean TCH < 3 m were recoded to natural grassland (3.2.1), polygons with mean TCH between 3 and 6 m were assigned to sclerophyllous vegetation (3.2.3), and polygons with mean TCH > 6 m were promoted to broadleaved forest (3.1.1). These thresholds were applied to decompose the transitional woodland–shrub class (3.2.4) and mixed forest (3.1.3) into their constituent components, and to reclassify sclerophyllous vegetation polygons (3.2.3) whose canopy height was inconsistent with a shrub-dominated structure. For mixed forest (3.1.3), accuracy assessment and spectral analysis revealed that the vast majority of polygons were characterized by structural signatures consistent with broadleaved rather than coniferous cover, suggesting that the mixed-forest label had been inherited from previous ancillary classifications without reflecting the actual canopy composition. All mixed-forest polygons were therefore recoded, with the herbaceous component recoded to natural grassland (3.2.1) and the arboreal component recoded to broadleaved forest (3.1.1), effectively eliminating the mixed-forest class from the final legend. Finally, across all natural vegetation classes, polygons with a dominant PBS value greater than 33, corresponding to bare soil, rock, or shadow classes in the PBS legend, were identified as spectrally inconsistent with any vegetated land cover and recoded into the appropriate non-vegetated class, including bare rock (3.3.2) or sparse vegetation (3.3.3), through photo-interpretation based on contextual information from high-resolution orthophotos.

Similarly, arable land polygons (2.1.1, 2.1.2.1) with mean TCH > 2 m were identified as potentially containing tree rows, windbreaks, olive groves, or orchards erroneously labelled as arable land, and were reclassified into proper natural vegetation classes through manual recoding through photointerpretation.

Manual reclassification was conducted using IMPACT Toolbox in multi-user mode, integrating AGEA 2019 orthophotos, Google Earth and Google Street View imagery, and Sentinel-2 multi-temporal composites. This approach was applied where classification errors could not be resolved through automatic or semi-automatic methods, either because the land cover types involved were spectrally indistinguishable at the resolution of Sentinel imagery or because correct class assignment required contextual interpretation of fine-scale spatial patterns. Wetland classes (4.1.1, 4.2.1) were extensively revised through photo-interpretation, as the confusion between non-alophilous and alophilous marsh vegetation, detected through accuracy assessment, could not be resolved spectrally. The two classes were separated based on their salinity context and vegetation composition, and water body components (5.1.2, 5.2.1) previously merged within wetland polygons were delineated and recoded separately. Permanent crop classes, vineyards (2.2.1), olive groves (2.2.3), and fruit trees (2.2.2), were similarly reviewed and corrected where spectral similarity with adjacent natural vegetation or other crop types had led to misclassification. Transitional and spatially heterogeneous environments, including the coastal zone, saline areas, and other ecotonal landscapes, required systematic manual revision due to their high fine-scale spatial variability and spectral complexity. The entire coastal zone was systematically reviewed to correctly differentiate beaches and sandy areas (3.3.1), bare rock and cliffs (3.3.2), sparse coastal vegetation (3.3.3), port infrastructures (1.2.3), and sclerophyllous coastal maquis (3.2.3). Saline areas (4.2.2) and their surrounding transitional environments were similarly revised to correctly separate active and abandoned salt pans from adjacent wetland and bare soil classes. Finally, a cleaning phase was conducted to resolve all polygons retaining only first- or second-level CORINE codes, as well as temporary mixed classes of bare soil and remaining tree cover, and the temporary unclassified urban polygons, OSM-derived built-up areas flagged during Step 1 as misclassified. For example, 98% of recoded bare soil polygons were assigned to sparse vegetation (3.3.3) and the other 2% to industrial or commercial areas (1.2.1), non-irrigated arable lands (2.1.1), or inland water bodies (5.1.2) based on contextual interpretation. This phase also included the resolution of temporary unclassified urban polygons, i.e., OSM-derived built-up areas flagged during Step 1 as misclassified based on their spectral inconsistency with any built-up surface.

3.4.2. Accuracy Assessment

Map accuracy was evaluated using a reference dataset of more than 11 thousand control points collected through two complementary strategies. A first subset of approximately 8500 points was generated randomly across the entire regional extent using a stratified random sampling approach [50], with a minimum inter-point distance of 500 m imposed to limit spatial autocorrelation. A second subset of approximately 3300 points was selected by expert operators through photo-interpretation. These points were chosen to maximize representativeness of each class and geographic coverage across the island, with particular attention to natural and semi-natural vegetation classes (CORINE classes 3, 4, and 5) and to classes underrepresented in the random sample. Although the inclusion of purposive points alongside the probability-based random sample does not strictly conform to a design-based estimator with fully known sampling probabilities as recommended by [51], purposive points were selected solely to fill geographic and thematic gaps in the random sample, targeting underrepresented classes and ensuring regional coverage, by photo-interpreters who had no involvement in the classification process and no knowledge of the map output. This design minimizes the risk of systematic bias in the accuracy estimate.

Both subsets were attributed by three trained photo-interpreters following a preliminary inter-calibration phase to ensure consistency in class assignment across operators. The inter-calibration phase consisted of independent attribution of a shared subset of reference points, followed by systematic discussion of discordant cases to reach consensus on interpretation criteria; formal interrater agreement statistics were not computed.

Point attribution was performed using the best available orthophoto for each area with an acquisition date close to 2020, either AGEA 2019 or 2022 orthophotos or Google Earth imagery, integrated with Sentinel-2 multi-temporal composites and, where available, Google Street View. The interpretation protocol distinguished two cases depending on the spatial homogeneity of the enclosing polygon: where the polygon containing the point was characterized by a homogeneous land cover, defined as at least 80% of the polygon area occupied by the same class, the point was attributed based on the overall polygon content; where the polygon contained multiple land cover types, attribution was performed at the point level, considering a 20 m buffer around the point. This approach serves a dual purpose: polygon-level attribution evaluates the thematic accuracy of the classification, while point-level attribution in heterogeneous polygons allows the identification of segmentation errors, cases where the polygon boundary fails to correctly delineate spectrally or thematically distinct land cover units. The full dataset was subsequently reviewed to remove duplicates and clusters of points located too close to each other (<50 m), retaining only the most representative point per cluster to avoid oversampling of spatially autocorrelated areas. The final validated dataset comprised 11,575 control points.

Accuracy assessment followed good practice recommendations for stratified sampling and area-weighted estimation [51]. The overall weighted accuracy is then computed as the sum of the weighted correctly classified points divided by the sum of all weighted points, yielding an area-weighted estimate of map accuracy consistent with the stratified estimator of [51,52]:

$$\hat{O} = \sum_{i=1}^{q} W_i \hat{U}_i \quad (1)$$

where q is the number of classes, $W_i = a_i/100$ is the mapped area proportion of class i, and $\hat{U}_i = n_{ii}/n_i$ is the proportion of correctly classified sample units in class i, with n_{ii} being the number of correctly classified points and n_i being the total number of reference points for class i. Furthermore, for each class, the 95% confidence intervals of User Accuracy were estimated following [51]. This weighting scheme ensures that accuracy estimates reflect the actual class distribution in the map rather than the sampling density, preventing dominant classes from disproportionately influencing the overall accuracy figure.

3.5. Burned Areas Classification

Burned area mapping was carried out using a multi-temporal Sentinel-2 MSI time series approach combined with a Random Forest classifier, following the methodology described in detail in [38]. Candidate burned pixels were identified through a rule-based algorithm applied to the dual-date Mid-Infrared Bi-Spectral Index (dMIRBI) and refined using spectral–temporal metrics and topographic variables to reduce commission errors related to terrain shadow effects. The final product was restricted to natural land cover classes as defined by the LULC map. Validation yielded a Dice Coefficient of 91.8%, substantially outperforming EFFIS (DC = 79.9%) and MODIS MCD64A1 (DC = 29.8%).

4. Results

4.1. The Land Cover Map

The Sardinia LULC map for the reference year 2020 covers the entire regional territory of approximately 24,090 km^2. The classification legend comprises 35 classes, all defined at the third and selected fourth levels of the CORINE Land Cover (CLC) hierarchy and reported in Table 1. While maintaining the overall structure of the standard CLC legend, several modifications were introduced to better reflect the spectral and structural characteristics of the Sardinian landscape and to align the classification with a land-cover-based rather than land-use-based approach.

The most significant modification from the standard CLC legend concerns the urban fabric classes: class 1.1.1, originally defined as continuous urban fabric based on the degree of impervious surface cover, was redefined as “Built-up surfaces”, encompassing exclusively individual building footprints derived from high-resolution ancillary datasets; class 1.1.2, originally discontinuous urban fabric, was redefined as “Other artificial surfaces”, grouping all remaining impervious surfaces not corresponding to buildings or linear infrastructure. Several classes present in the 2008 Land Use Map of Sardinia and in the standard CLC legend were not included in the classification, as they cannot be reliably discriminated using spectral information alone at the regional scale. These include permanent grasslands (2.3.1), which are spectrally indistinguishable from natural grasslands and rainfed arable land without ancillary land-use information; agroforestry areas (2.4.4), which were instead decomposed into their constituent land cover components; and mixed forest (3.1.3), whose broadleaved and coniferous components were individually assigned to classes 3.1.1 and 3.1.2, respectively, given that the map's fine MMU allows their spatial discrimination. Similarly, the transitional woodland–shrub class (3.2.4) was decomposed into its herbaceous and arboreal components and is not present in the final legend. A burned area class (3.3.4) was added as a complementary thematic layer, not present in the standard CLC legend, derived from the dedicated mapping study described in Section 3. The complex cultivation patterns class (2.4.2) is retained in the legend but covers a very limited extent. It was assigned manually by operators to polygons presenting a heterogeneous mix of crop types that could not be interpreted univocally at the map's spatial resolution. This class is considered a practical solution for spatially unresolvable mixed parcels and is expected to be progressively reduced in future map updates through sub-segmentation and more detailed field verification.

The land cover map (Figure 9), produced after pixel-based classification, image segmentation, infrastructure overlay, and reclassification operations, comprised 10,424,273 polygons. The spatial resolution of the map is defined by a minimum mapping unit (MMU) of 400 m^2, corresponding to 4 pixels of the Sentinel imagery at 10 m resolution, which constitutes the primary driver of the map's geometric detail. However, since high-resolution ancillary vector datasets, including DBGT building footprints, road networks, and OSM layers, were integrated into the map through geometric overlay operations, the final product also contains polygons with areas below 400 m^2, whose geometry is determined by the native resolution of the ancillary data rather than by the satellite imagery processing parameters.

Figure 9. Illustration of the three main steps of the LULC mapping workflow over a sample area in the Sulcis-Iglesiente region (south-western Sardinia). (**A**): pixel-based classification output, showing the typical salt-and-pepper effect resulting from pixel-level spectral variability. (**B**): result after image segmentation, polygon pre-labelling, and geometric overlay of road networks and building footprints; the segmentation effectively removes the salt-and-pepper effect, while the infrastructure overlay introduces the road network. (**C**): final map after the full reclassification cycle, where generic second-level

CORINE classes (3.1, 3.2, 3.3) and the temporary tree cover class are resolved into their appropriate third-level categories, and the transitional woodland–shrub class (3.2.4) is decomposed into its constituent components. Permanent crop classes are refined and corrected, and tree rows previously labelled as arable land are recovered as distinct land cover units.

The dominant land cover classes in terms of areal extent (Figure 10) are broadleaved forest (3.1.1, ~674,825 ha, 28.0% of the regional territory) and sclerophyllous vegetation (3.2.3, ~609,292 ha, 25.3%), together accounting for more than half of the island's surface and reflecting the prevalence of Mediterranean maquis and oak-dominated woodlands across the Sardinian landscape. Non-irrigated arable land (2.1.1) represents the largest agricultural class (~624,198 ha, 25.9%), considerably exceeding natural grassland (3.2.1, ~153,164 ha, 6.4%). This disproportion partly reflects the regional context, characterized by a deeply rooted agro-pastoral land use tradition where the boundary between cultivated and natural grassland is often gradual and not clearly defined on the ground. Olive groves (2.2.3) cover approximately 58,347 ha (2.4%), representing the most extensive permanent crop class. Built-up surfaces (1.1.1) cover approximately 14,375 ha (0.6%). Among water-related classes, coastal lagoons (5.2.1) represent the most extensive (~12,520 ha), consistent with Sardinia's notable concentration of lagoonal environments along its western and southern coastlines.

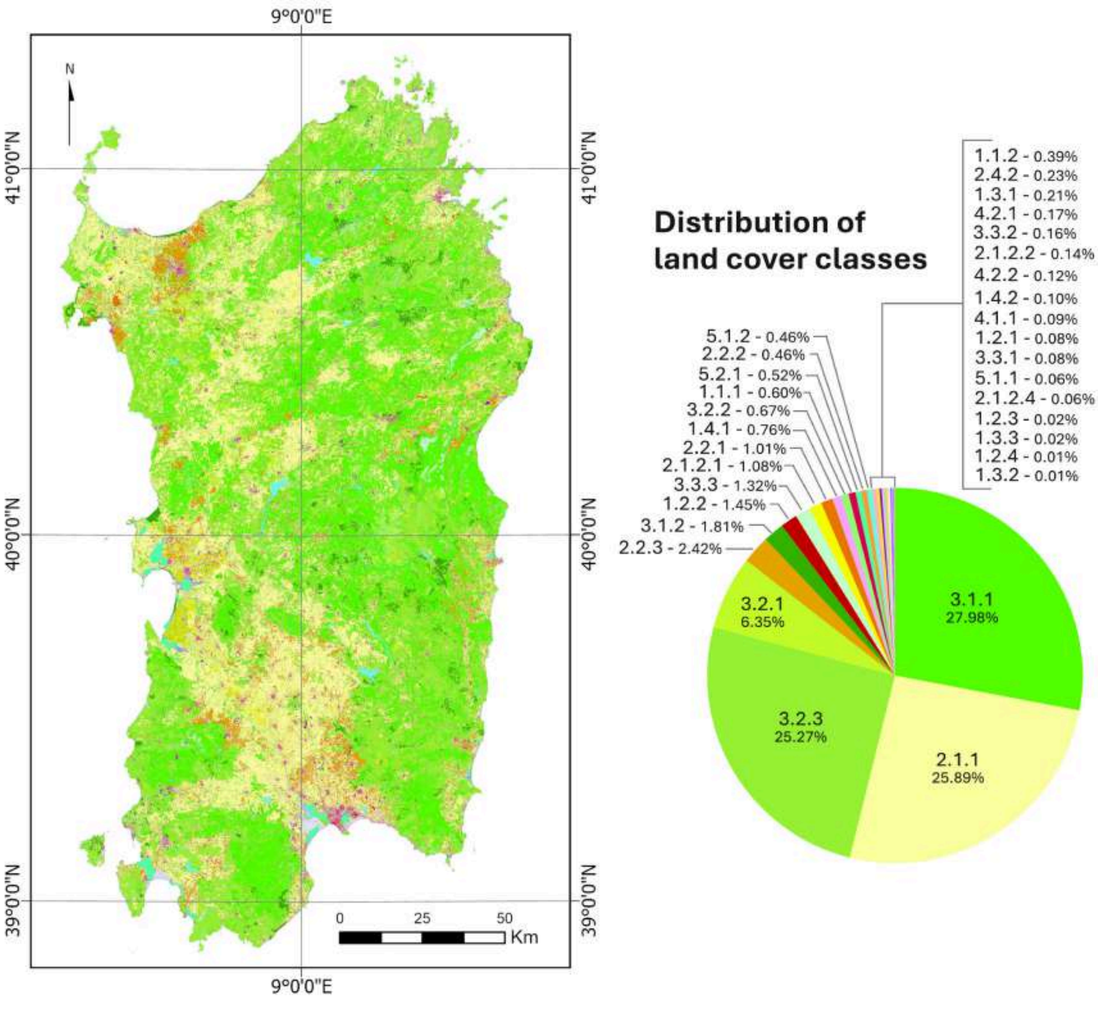

Figure 10. Land cover map of Sardinia for the reference year 2020 (**left**) and percentage areal distribution of the 35 classified land cover classes (**right**). The pie chart highlights the dominance of broadleaved forest (3.1.1, 27.98%), sclerophyllous vegetation (3.2.3, 25.27%), and non-irrigated arable

land (2.1.1, 25.89%), which together account for approximately 79% of the island's surface, while the remaining 21% is distributed across 31 classes of varying extent, several of which cover less than 0.5% of the territory.

Several classes occupy a very limited extent, including salines (4.2.2, ~2878 ha), dump sites (1.3.2, ~289 ha), and beaches and sandy areas (3.3.1, ~1842 ha). The complex cultivation patterns class (2.4.2), as previously discussed, covers approximately 5503 ha and represents a residual category of spatially unresolvable mixed agricultural parcels. Burned areas (3.3.4) are not included in this areal summary as they are provided as a complementary thematic layer rather than a standard map class.

4.2. Accuracy Assessment

The overall weighted accuracy of the preliminary map, evaluated prior to any reclassification operation, was 69.3%, reflecting the cumulative effect of errors inherited from ancillary datasets and limitations of the pixel-based classification. Following the full iterative reclassification cycle, the overall weighted accuracy of the final map reached 82.4%, representing an improvement of 13.1 percentage points and demonstrating the effectiveness of the accuracy-driven refinement workflow.

The per-class accuracy values, sample sizes (n_i), and 95% confidence intervals derived from the weighted confusion matrix (Figure 11) show a heterogeneous distribution across the 34 validated classes. Per-class sample sizes and User Accuracy confidence intervals are reported in Table 6.

Table 6. Per-class sample size (n_i), User Accuracy (UA), standard error (SE (UA)), and 95% confidence interval (95% CI) for the 34 validated classes of the Sardinia LULC Map 2020, estimated following [51].

Accuracy Assessment—OA = 82.44% ± 0.67% (95% CI)—n = 11,575 Points				
Class	**n_i (Sample Size)**	**User Accuracy**	**SE (UA)**	**95% CI (UA)**
1.1.1	35	88.83%	5.40%	±10.59%
1.1.2	49	54.10%	7.19%	±14.10%
1.2.1	57	54.97%	6.65%	±13.03%
1.2.2	174	98.20%	1.01%	±1.98%
1.2.3	63	60.97%	6.20%	±12.14%
1.2.4	37	50.16%	8.33%	±16.33%
1.3.1	51	59.88%	6.93%	±13.59%
1.3.2	42	6.32%	3.80%	±7.45%
1.3.3	48	7.52%	3.85%	±7.54%
1.4.1	79	66.43%	5.35%	±10.48%
1.4.2	53	41.04%	6.82%	±13.37%
2.1.1	3040	84.29%	0.66%	±1.29%
2.1.2.1	296	88.44%	1.86%	±3.65%
2.1.2.2	62	100.00%	0.00%	±0.00%
2.1.2.4	61	61.51%	6.28%	±12.31%
2.2.1	129	63.04%	4.27%	±8.36%
2.2.2	64	40.76%	6.19%	±12.13%
2.2.3	181	71.60%	3.36%	±6.59%
2.4.2	33	34.95%	8.43%	±16.52%
3.1.1	1348	73.19%	1.21%	±2.37%
3.1.2	219	64.12%	3.25%	±6.37%
3.2.1	768	51.67%	1.80%	±3.54%
3.2.2	295	30.66%	2.69%	±5.27%
3.2.3	2200	81.89%	0.82%	±1.61%
3.3.1	214	53.91%	3.42%	±6.69%
3.3.2	162	25.00%	3.41%	±6.69%
3.3.3	240	47.69%	3.23%	±6.33%

Table 6. *Cont.*

Accuracy Assessment—OA = 82.44% ± 0.67% (95% CI)—n = 11,575 Points				
Class	**n_i (Sample Size)**	**User Accuracy**	**SE (UA)**	**95% CI (UA)**
4.1.1	237	45.80%	3.24%	±6.36%
4.2.1	232	39.93%	3.22%	±6.32%
4.2.2	78	84.49%	4.13%	±8.09%
5.1.1	201	53.00%	3.53%	±6.92%
5.1.2	232	91.99%	1.79%	±3.50%
5.2.1	233	42.99%	3.25%	±6.37%
5.2.3	362	99.90%	0.17%	±0.33%

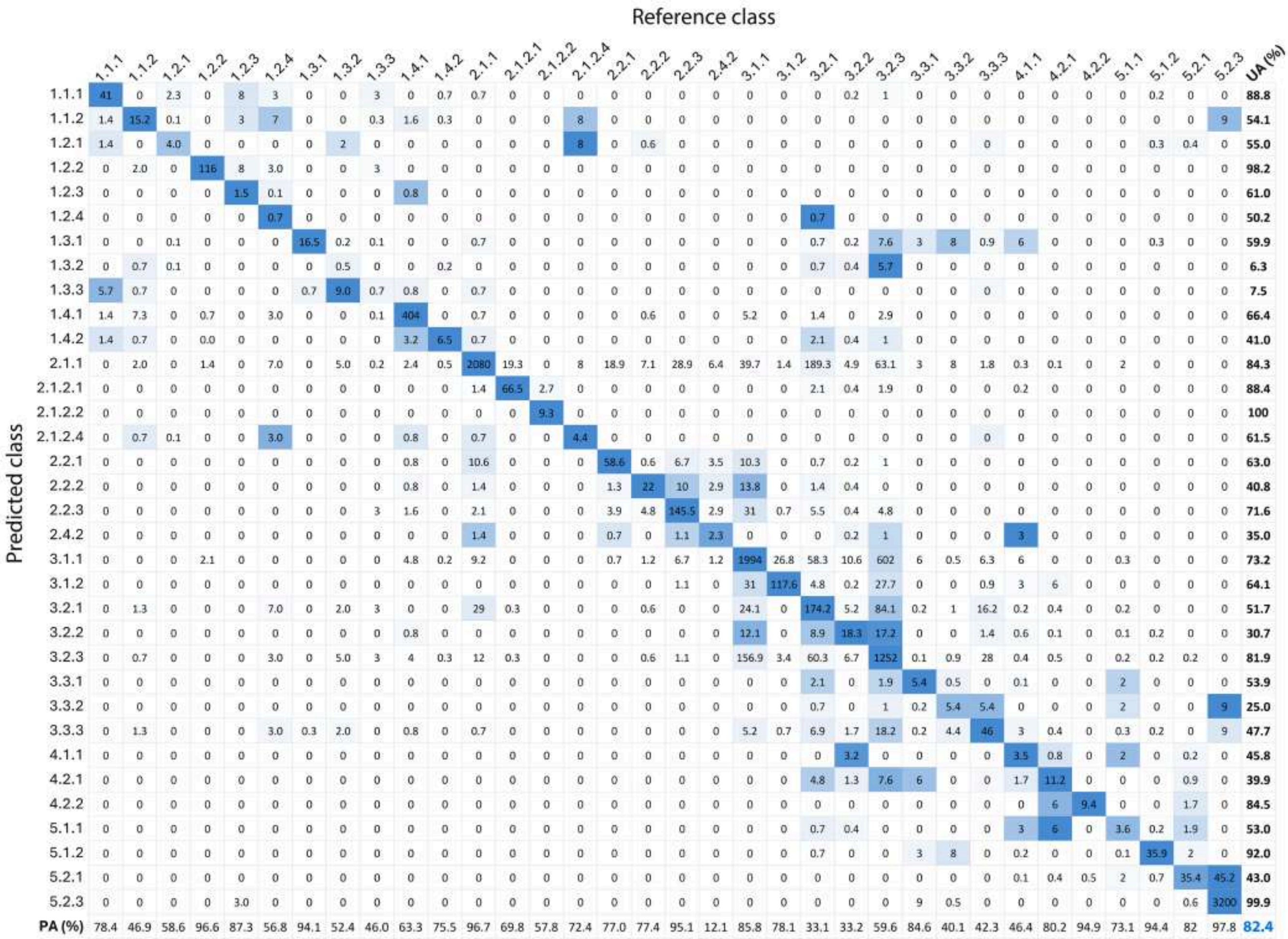

Figure 11. Weighted confusion matrix of the final Sardinia LULC map, computed at the third and selected fourth levels of the CLC legend using 11,575 control points. Rows represent predicted classes and columns represent reference classes. Cell values correspond to weighted point counts, with darker shading indicating higher values. User accuracy (UA) and producer accuracy (PA) are reported for each class in the rightmost column and bottom row, respectively. Overall weighted accuracy is 82.4%.

Five classes have fewer than 50 validation points: built-up surfaces (1.1.1, n = 35), airports and heliports (1.2.4, n = 37), dump sites (1.3.2, n = 42), construction sites (1.3.3, n = 48), and complex cultivation patterns (2.4.2, n = 33). Their accuracy estimates should be interpreted with caution, as the sample may not be sufficient to provide a statistically robust accuracy estimate. For the same reason, with only 62 validation points, rice fields (2.1.2.2) showed unlikely perfect user accuracy (UA = 100%) and high producer accuracy (PA = 77.4%).

That said, the very distinctive flooding signal captured by the NDFI time series suggests that true accuracy is likely to remain high, even if marginally lower than reported.

Among the best-performing classes, road and rail networks (1.2.2) achieved the highest accuracy (UA = 98.2% ± 2.0%, PA = 96.6%), benefiting from the direct integration of high-resolution ancillary vector data from DBGT and OSM. Very high UA values were also recorded for water bodies (5.1.2, UA = 91.99% ± 3.5%) and irrigated arable lands (2.1.2.1, UA = 88.44% ± 3.6%).

Sclerophyllous vegetation (3.2.3) achieved a notably high user accuracy (UA = 81.9% ± 1.6%), though with a lower producer accuracy (PA = 59.6%), indicating that while classified polygons are largely correct, a significant fraction of sclerophyllous vegetation in the reference data was assigned to other classes, primarily broadleaved forest (3.1.1).

The lowest user accuracies were recorded for dump sites (1.3.2, UA = 6.3% ± 7.5%) and construction sites (1.3.3, UA = 7.5% ± 7.5%). These classes represent a particular challenge in land cover mapping because they are defined primarily by land use rather than by a distinctive spectral signature. Dump sites and construction areas can exhibit a wide range of surface types, from bare soil to artificial materials, that are spectrally indistinguishable from other classes such as mineral extraction sites, bare soils, or artificial surfaces. Furthermore, both classes are highly dynamic in time, with sites frequently opening, closing, or changing their surface characteristics between the acquisition date of the ancillary datasets used for classification and the reference year of the map, making it difficult to maintain an up-to-date and complete inventory of these features even from authoritative data sources.

Bare rock (3.3.2) also performed poorly (UA = 25.0% ± 6.7%, PA = 14.5%), with reference pixels frequently misclassified as mineral extraction sites or non-irrigated arable land, reflecting the difficulty of discriminating exposed rock from other bright, sparse surfaces at 10 m resolution. Non-sclerophyllous shrub vegetation (3.2.2) showed UA = 30.7% ± 5.3% and PA = 33.2%, consistent with the high internal heterogeneity of this class, which encompasses a wide range of non-sclerophyllous formations, including riparian shrubs, brambles, and deciduous thickets, frequently confused with broadleaved forest and sclerophyllous vegetation.

The most significant sources of confusion were observed among spectrally similar natural vegetation classes. Sclerophyllous vegetation (3.2.3) showed the largest absolute confusion, with a substantial portion of its reference pixels classified as broadleaved forest (3.1.1), a well-documented challenge in Mediterranean environments where dense maquis and open forest share overlapping spectral signatures [53,54].

Natural grassland (3.2.1) showed a particularly low producer accuracy (PA = 33.1%) despite a user accuracy of 51.7% ± 3.5%, indicating significant omission errors, with reference pixels frequently absorbed by non-irrigated arable land (2.1.1) and sclerophyllous vegetation (3.2.3). The confusion with non-irrigated arable land is particularly difficult to overcome using spectral information alone: in the Mediterranean climate of Sardinia, natural grasslands and rainfed winter and spring crops share virtually identical NDVI temporal dynamics; both exhibit active growth during the wet season and senesce during the summer dry period, making their phenological profiles nearly indistinguishable in multi-temporal Sentinel-2 analysis. This confusion represents a fundamental limitation of spectral classification approaches in Mediterranean environments, further compounded by the fact that the two classes are often difficult to distinguish even through photo-interpretation, depending on the acquisition date of the available high-resolution imagery; e.g., a green field in winter or early spring can appear identical regardless of whether it is a natural grassland or a crop.

Among permanent crops, olive groves (2.2.3) performed best (UA = 71.6% ± 6.6%, PA = 72.4%), while fruit trees (2.2.2) showed lower accuracy (UA = 40.8% ± 12.1%, PA = 57.8%) due to confusion with other arboreal classes. Vineyards (2.2.1) achieved UA = 63.0% ± 8.4% and PA = 69.8%, with the main confusion occurring with non-irrigated arable land.

The relatively moderate accuracy of this class reflects the high variability of viticulture practices in Sardinia, which poses a significant challenge for spectral classification. Vine management techniques vary considerably across the island, including differences in pruning periods, row spacing, training systems, and canopy architecture, resulting in a wide range of spectral and phenological responses that do not conform to a single temporal NDVI signature. The diversity of grape varieties cultivated in Sardinia further amplifies this variability. Additionally, a large proportion of Sardinian vineyards are small, low-productivity parcels embedded within complex agricultural mosaics, where their limited spatial extent and proximity to other crop types make clean spectral separation particularly difficult, and where the polygon boundaries of the map may not fully capture the fine-scale spatial heterogeneity of the agricultural landscape.

Wetland classes represent one of the most challenging environments for remote sensing-based land cover mapping, due to their high spatial heterogeneity, the gradual and often indistinct transitions between adjacent vegetation types and water bodies, and their strong seasonal dynamics [55,56]. Against this background, halophilous marsh vegetation (4.2.1) achieved surprisingly high accuracy (UA = 84.5% ± 8.1%, PA = 94.9%), a result that can be attributed in large part to the extensive manual reclassification effort dedicated to this class, which allowed the correct separation of halophilous from non-halophilous vegetation based on contextual interpretation of vegetation composition not resolvable through spectral analysis alone. Non-halophilous marsh vegetation (4.1.1), on the other hand, showed lower accuracy (UA = 39.9% ± 6.3%, PA = 11.2%), confirming the intrinsic difficulty of mapping this class: as a transitional and fragmented environment between open water and terrestrial natural vegetation, it is characterized by exceptionally high internal heterogeneity in terms of species composition, water saturation, and canopy structure, which results in highly variable spectral responses that overlap with multiple adjacent classes and remain difficult to resolve even through photointerpretation.

5. Discussion

The complexity of the Sardinian landscape, characterized by high environmental heterogeneity, a deeply rooted agro-pastoral land use tradition, fragmented agricultural systems, and a diverse mosaic of natural and semi-natural habitats, poses specific challenges for land cover mapping that existing regional and global products are not designed to address. The fine-scale spatial variability of the island's land cover, the spectral similarity among many of its dominant classes, and the need for thematic detail relevant to local governance and environmental monitoring all require an approach that goes beyond what is achievable through fully automated global or continental mapping workflows applied at coarse spatial resolution or with simplified classification legends. This study was conceived precisely to fill this gap: to provide a thematically detailed, spatially accurate, and, crucially, regularly updatable land cover map specifically designed to support local-scale environmental monitoring, water resource management, and territorial governance. Unlike global and continental products, which prioritize spatial coverage and automation at the expense of thematic detail, and unlike the previous regional cartography, which offered a rich legend but was produced through manual photointerpretation on outdated imagery and has remained static since 2008 [32,33], the Sardinia LULC map is designed as a dynamic product that can be updated on an annual basis as new Sentinel imagery becomes available while maintaining the thematic consistency and spatial resolution required for operational use at the local scale.

The advantages of this approach become particularly evident when compared visually with some of the existing land cover products available for the Sardinian territory (Figures 12–14). Global and continental products (e.g., ESA WorldCover) show high spatial resolution but simplified legends, which limit their thematic detail in complex and heterogeneous landscapes such as Sardinia. CLC2018 and the 2008 Sardinia Land Use Map, by contrast, have rich legends, but their coarser minimum mapping units prevent the delineation of fine-scale spatial heterogeneity. In both cases, these limitations result in a more generalized spatial representation, as illustrated in the sample area in northern Sardinia (Figures 13 and 14).

Figure 12. High-resolution satellite imagery (Esri World Imagery, © Esri, Maxar, Earthstar Geographics; ~0.5 m/pixel) of a coastal sample area in northern Sardinia (municipality of Valledoria), providing a reference for the actual land cover present on the ground for visual comparison with existing land cover products.

In contrast, the Sardinia LULC map combines a 10 m satellite-based spatial resolution with an MMU of 400 m^2 and a 35-class legend specifically adapted to the thematic and spectral complexity of the regional landscape, including classes not present in any of the above products, such as the distinction between halophilous and non-halophilous marsh vegetation, the separation of irrigated arable land from non-irrigated arable land, and the mapping of salines and coastal lagoons as distinct classes. The integration of high-resolution ancillary vector datasets (DBGT, OSM) further allows the delineation of individual building footprints, road networks, and infrastructure features at their native geometric precision, a level of spatial detail unattainable by purely satellite-based approaches at regional scale.

A second major strength is the iterative accuracy-driven refinement workflow, which produced a final overall weighted accuracy of 82.4% (95% CI: ±0.67%) across a legend of substantially higher thematic complexity than any existing global or continental product for the study area, a result that underscores the effectiveness of the iterative refinement approach in a heterogeneous Mediterranean landscape.

A third and particularly significant advantage is the operational updatability of the map. The Sardinia LULC map is designed as a dynamic product rather than a static cartographic snapshot: the availability of regular Sentinel-1 and Sentinel-2 acquisitions enables the systematic identification of land cover changes without the need to repeat the full classification workflow. Three complementary update strategies are foreseen: (i) geometric overlay of new polygons from updated ancillary datasets or dedicated classifications such as the annual burned area mapping [38]; (ii) reclassification of existing polygons without modifying their geometry, e.g., the annual update of the irrigated/non-irrigated arable land distinction by rerunning the phenological classifier on new Sentinel-2 time series; and (iii) detection of structural changes through pixel-level spectral difference analysis or re-segmentation of new Sentinel imagery within existing polygon boundaries, with flagged polygons submitted for targeted reclassification. Together, these strategies ensure that the map can be maintained as a continuously updated, temporally consistent record of the Sardinian land cover.

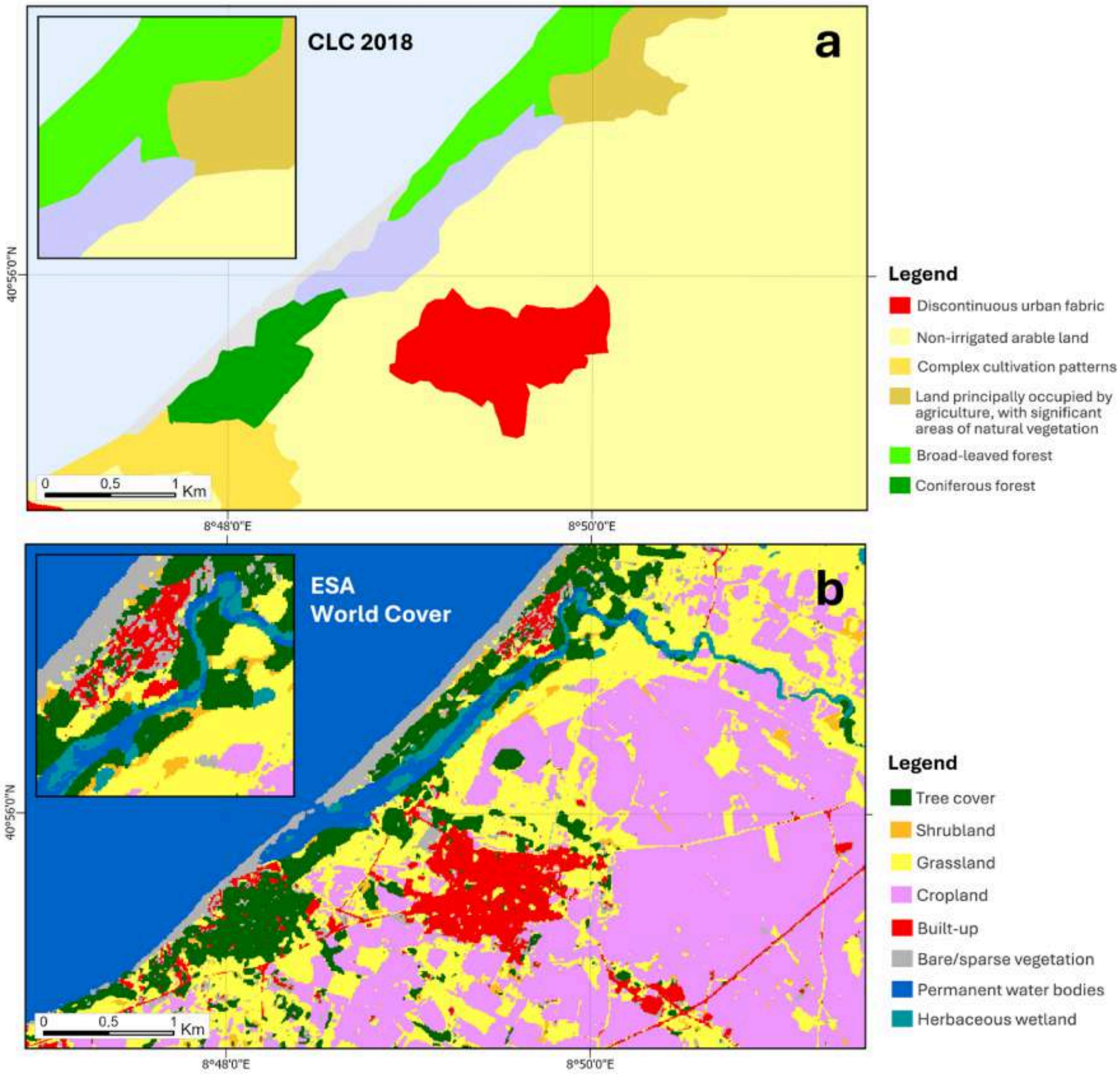

Figure 13. Visual comparison of existing land cover products over the same coastal sample area in northern Sardinia (municipality of Valledoria), shown in Figure 12, characterized by a complex mosaic of beaches, wetlands, agricultural lands, and urban fabric: (**a**) Copernicus CORINE Land Cover 2018 (CLC2018, 100 m resolution, MMU 25 ha), showing the coarse spatial generalisation imposed by the minimum mapping unit, which prevents the delineation of fine-scale landscape features; (**b**) ESA WorldCover 2020 (10 m resolution, 11 classes), which, despite its higher spatial resolution, fails to capture the thematic complexity of the area, merging ecologically distinct environments, including coastal wetlands and agricultural mosaics, into broad and undifferentiated classes. The insets highlight the zoom area indicated by the black rectangle, emphasising the loss of spatial and thematic detail in both products relative to the high-resolution reference imagery.

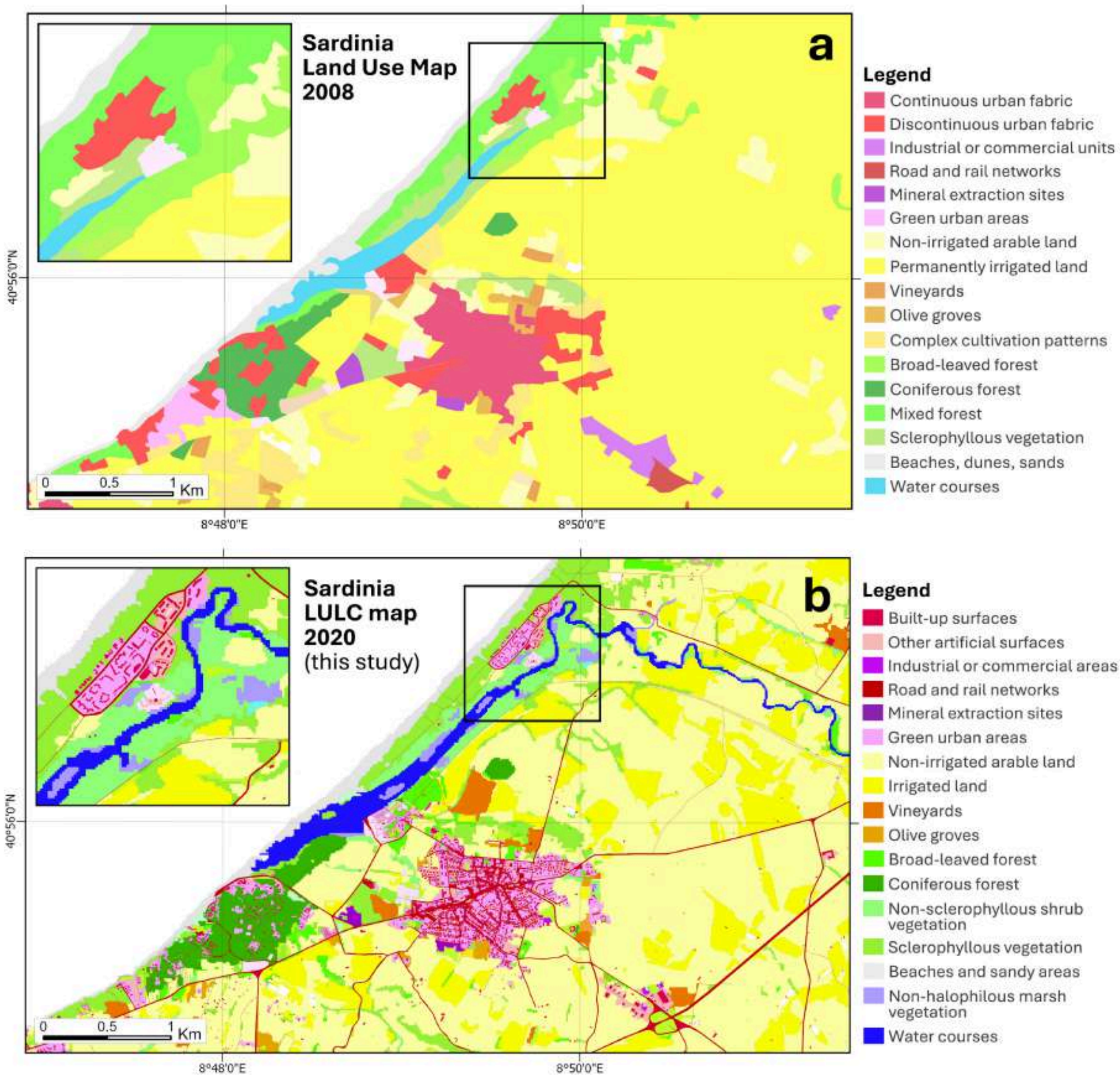

Figure 14. Visual comparison between the Sardinia Land Use Map 2008 (**a**) and the Sardinia LULC map 2020 produced in this study (**b**), over the same coastal sample area shown in Figures 12 and 13. The insets highlight the zoom area indicated by the black rectangle. Several improvements are immediately apparent. The geometric overlay of high-resolution building footprints and road networks from DBGT and OSM datasets introduces a level of spatial detail in the delineation of urban and infrastructure features that are entirely absent in the 2008 map, where the urban fabric is represented as large, undifferentiated polygons. The distinction between irrigated and non-irrigated arable land represents a further critical improvement: in the 2008 map, the majority of the agricultural area is classified as permanently irrigated land, a generalization that does not reflect the actual irrigation practices on the ground; the 2020 map, by contrast, discriminates between irrigated and non-irrigated parcels on the basis of multi-temporal NDVI dynamics, producing a more realistic and operationally useful representation of the agricultural landscape.

Despite the overall satisfactory performance of the map, several structural limitations persist. Classes defined by land use rather than land cover (dump sites, construction areas, transport infrastructure) remain dependent on the completeness and currency of ancillary datasets, a constraint that cannot be resolved through spectral classification alone. The confusion between spectrally similar natural classes (grassland versus arable land, maquis versus open woodland) and the complexity of wetland environments represent inherent limitations of optical remote sensing in heterogeneous Mediterranean landscapes. These limitations are not fully resolvable within the current framework and define the primary targets for improvement in future map updates, including the integration of higher-resolution ancillary datasets, additional field surveys for wetland classes, and the progressive adoption of deep learning classifiers as the labelled training dataset grows.

More broadly, the dependence on ancillary sources of heterogeneous temporal consistency is a structural characteristic of cascade classifier architectures that deserves explicit consideration. In the present workflow, the ancillary datasets used, DBGT (2022), OSM (December 2022), CLC2018, and the 2008 Land Use Map, do not coincide precisely with the 2020 reference year, introducing potential temporal inconsistencies, particularly for dynamic land cover classes such as construction sites, urban expansion areas, and agricultural transitions. In the present workflow, these limitations are addressed at multiple levels. Within the pixel-based classification itself, Step 1 incorporates post-assignment correction rules that systematically detect and recode inconsistencies between ancillary-derived labels and satellite-derived spectral and SAR indicators, using threshold-based conditions to identify pixels whose assigned class is incompatible with their observed spectral response. Step 2 extends this logic to the agricultural domain, where dedicated correction classifiers identify and remove components from the agricultural mask surfaces, including water bodies, wetlands, and persistently unvegetated areas, whose spectral signatures are incompatible with any agricultural land cover class, recovering both commission errors from Step 1 and omission errors from earlier classification stages. At the polygon level, the iterative reclassification cycle constitutes a further error management mechanism: by computing confusion matrices at multiple stages of the production process, it identifies classes where propagated errors from ancillary sources are most severe and directs targeted correction efforts accordingly. Together, these three levels of error control do not eliminate the structural dependence on ancillary source quality and temporal inconsistencies, but provide a tractable and operationally viable strategy for detecting, localizing, and progressively reducing propagated errors in a regional-scale mapping context where temporally consistent, comprehensive ancillary datasets are unavailable.

The temporal specificity and territorial transferability of the classification is a further concern. The map refers to the reference year 2020, and the spectral and phenological thresholds adopted in the pixel-based classification were calibrated on that specific year and on the environmental, climatic, and agronomic characteristics of Sardinia. For most land cover classes, the temporal specificity does not represent a significant concern, as the map is designed to be updated through change detection rather than by repeating the full classification cycle. For the irrigated arable land class, however, which is reclassified annually using updated Sentinel-2 time series, the robustness of the classification criteria across years with different climatic conditions deserves consideration. The criteria adopted are based on relative NDVI trends and amplitude thresholds rather than absolute values, making them intrinsically more robust to inter-annual climatic variability; a field under irrigation will consistently exhibit a significant and sustained NDVI increase during summer regardless of the reference year.

More broadly, the workflow is not designed to be directly transferable to other regions without substantial adaptation. The classification thresholds, the hierarchical priority scheme of the ancillary datasets, the agricultural classification criteria, and the reclassification rules were all calibrated based on expert knowledge of the Sardinian landscape, its dominant land cover types, local agronomic practices, and the specific characteristics of the available ancillary datasets. This context-specificity is not a limitation in the conventional sense, but rather an intrinsic consequence of the level of thematic detail and accuracy that the approach achieves: adapting the classification model to the study area is precisely what allows the map to capture distinctions, such as the separation of irrigated crops from rainfed crops, the diversity of permanent crop types, or the fine-scale mosaic of natural vegetation, that no globally transferable automated workflow currently achieves at this spatial and thematic resolution. What is transferable is not the specific parameters, but the methodological framework: the combination of multi-source ancillary data integration, iterative spectral consistency correction, phenology-driven agricultural classification, and accuracy-driven refinement represents a general approach that can be adapted to other Mediterranean or complex heterogeneous landscapes, provided that equivalent ancillary datasets and local expert knowledge are available.

6. Conclusions

This study presents the first high-resolution, satellite-based land cover map of Sardinia for the reference year 2020, produced through a semi-automatic workflow combining multi-temporal Sentinel-1 and Sentinel-2 imagery, high-resolution ancillary geospatial datasets, and an iterative accuracy-driven refinement cycle. The resulting map, comprising 35 classes defined at the third and selected fourth levels of an adapted CORINE Land Cover legend, with a minimum mapping unit of 400 m^2 and an overall weighted accuracy of 82.4%, represents a substantial advancement over all existing regional and global land cover products in terms of spatial detail, thematic richness, and temporal currency. By bridging the gap between the thematic depth of traditional photointerpretation-based cartography and the scalability and updatability of modern satellite-based mapping approaches, it provides an operational tool for environmental monitoring, water resource management, agricultural policy, and territorial governance at the local scale. The operational nature of this contribution is confirmed by its active use within the institutional framework of ADIS (Agenzia del Distretto Idrografico della Sardegna) for the preparation of the River Basin Management Plan for Sardinia, as required by the EU Water Framework Directive (2000/60/EC), one of the primary instruments of water resource governance in the European Union.

Despite these achievements, significant challenges remain. The spectral similarity among several dominant land cover classes represents a fundamental constraint of spectral classification in Mediterranean environments that cannot be fully overcome without the integration of additional data sources or field survey information. Wetland classes remain difficult to map reliably through remote sensing and photointerpretation alone, and their accurate delineation would require systematic in situ ecological surveys. The dependence on ancillary datasets of variable currency and completeness, and the inherent limitations of land-use-defined classes in a land-cover-based classification framework represent further sources of residual uncertainty that future work should address.

Several directions are foreseen for the continuation and improvement of this work. The most immediate priority is the annual updating of the map using the strategies described in Section 5, geometric overlay of new ancillary data, reclassification of existing polygons through updated phenological classifiers, and detection of structural changes through spectral difference analysis and re-segmentation of new Sentinel imagery, transforming the map from a static product into a continuously maintained, temporally consistent record of the Sardinian land cover. The integration of additional high-resolution datasets specifically targeted at problematic classes, such as field-collected floristic and ecological data for wetland environments, or updated cadastral information for agricultural and urban classes, is expected to yield significant accuracy improvements in future map versions. This process is already underway, as the 2025 update is in production, with three components already implemented: geometric overlay of updated building footprints and road network from OSM, reclassification of irrigated and non-irrigated arable land using new Sentinel-2 phenological time series, and detection of structural land cover changes through spectral difference analysis on new Sentinel acquisitions.

Finally, since no pre-existing labelled training dataset is available at the thematic detail required by the 35-class legend, the Sardinia LULC map represents a valuable training resource for future machine learning-based classification models. Its combination of thematic richness, regional validation, and fine-scale class distinctions, unavailable in any existing global or continental product for Mediterranean environments, provides an ideal foundation for developing supervised or deep learning classifiers capable of producing annually updated land cover maps in a fully or semi-automated manner, representing a natural evolution of the operational framework established in this study.

Supplementary Materials: The following supporting information can be downloaded at: https://www.mdpi.com/article/10.3390/land15081461/s1, Figure S1: Habitat map of Sardinia with complete legend from [35]; Figure S2: Pie charts showing the percentage surface area of habitats according to [35]. The larger pie chart (bottom right) summarizes all habitat categories, including an aggregated class "Other" that groups habitats with an extent lower than 1% of the total Sardinian surface. These minor categories are presented in greater detail in the smaller pie chart (top left), where habitats with an individual extent < 0.10% are further grouped into "Other minor classes".

Author Contributions: Conceptualization, C.C., D.S., F.D. and M.T.M.; methodology, C.C., D.S., H.I.G.G.D., F.D. and M.T.M.; software, D.S. and F.D.; validation, C.C., D.S., H.I.G.G.D. and M.T.M.; formal analysis, D.S.; investigation, D.S., F.D., H.I.G.G.D., P.L. and P.B.; resources, D.S., F.D., P.L., P.B. and M.T.M.; data curation, D.S., F.D. and H.I.G.G.D.; writing—original draft preparation, C.C.; writing—review and editing, D.S., F.D., H.I.G.G.D. and M.T.M.; visualization, C.C. and A.M.; supervision, D.S. and M.T.M.; project administration, P.L., P.B. and M.T.M.; funding acquisition, P.L., P.B. and M.T.M. All authors have read and agreed to the published version of the manuscript.

Funding: This work was supported by the Italian National PhD Program in Earth Observation, funded by the European Union—NextGenerationEU under the Italian National Recovery and Resilience Plan (NRRP), and by a research project named 'Sardinia Land Cover Mapping' [grant number F23C23000160005], in collaboration with the Regione Autonoma della Sardegna, Servizio Tutela e Gestione delle Risorse Idriche, Vigilanza sui Servizi Idrici e Gestione delle Siccità—Direzione generale Agenzia Regionale del distretto Idrografico della Sardegna.

Data Availability Statement: The datasets presented in this article are not readily available because the data are part of an ongoing study. Requests to access the datasets should be directed to https://www.sardegnageoportale.it/.

Acknowledgments: The authors acknowledge the support of Sapienza University of Rome and the Regione Autonoma della Sardegna for providing the institutional and collaborative framework within which this research was carried out.

Conflicts of Interest: Author Alberto Masala is employed by the company Sky Survey System di Alberto Masala & C. S.A.S. The remaining authors declare that the research was conducted in the absence of any commercial or financial relationships that could be construed as a potential conflict of interest.

References

1. Ulmas, P.; Liiv, I. Segmentation of Satellite Imagery using U-Net Models for Land Cover Classification. *arXiv* **2020**, arXiv:2003.02899. [CrossRef]
2. Tufail, R.; Tassinari, P.; Torreggiani, D. Assessing feature extraction, selection, and classification combinations for crop mapping using Sentinel-2 time series: A case study in northern Italy. *Remote Sens. Appl.* **2025**, *38*, 101525. [CrossRef]
3. Zhang, W.; Yang, X.; Yuan, Z.; Chen, Z.; Xu, Y. A Framework for Fine-Grained Land-Cover Classification Using 10 m Sentinel-2 Images. *Remote Sens.* **2024**, *16*, 390. [CrossRef]
4. Macarringue, L.S.; Bolfe, É.L.; Pereira, P.R.M. Developments in Land Use and Land Cover Classification Techniques in Remote Sensing: A Review. *J. Geogr. Inf. Syst.* **2022**, *14*, 1–28. [CrossRef]
5. Jocea, A.F.; Porumb, L.; Necula, L.; Raducanu, D. Sentinel-2 Land Cover Classification: State-of-the-Art Methods and the Reality of Operational Deployment—A Systematic Review. *Sustainability* **2025**, *17*, 10324. [CrossRef]

6. Zhang, X.; Liu, L.; Zhao, T.; Zhang, W.; Guan, L.; Bai, M.; Chen, X. GLC_FCS10: A global 10 m land-cover dataset with a fine classification system from Sentinel-1 and Sentinel-2 time-series data in Google Earth Engine. *Earth Syst. Sci. Data* **2025**, *17*, 4039–4062. [CrossRef]
7. Vuolo, F.; Neuwirth, M.; Immitzer, M.; Atzberger, C.; Ng, W.T. How much does multi-temporal Sentinel-2 data improve crop type classification? *Int. J. Appl. Earth Obs. Geoinf.* **2018**, *72*, 122–130. [CrossRef]
8. Wulder, M.A.; Coops, N.C.; Roy, D.P.; White, J.C.; Hermosilla, T. Land cover 2.0. *Int. J. Remote Sens.* **2018**, *39*, 4254–4284. [CrossRef]
9. Herrero, H.V.; Southworth, J.; Bunting, E.; Kohlhaas, R.R.; Child, B. Integrating surface-based temperature and vegetation abundance estimates into land cover classifications for conservation efforts in savanna landscapes. *Sensors* **2019**, *19*, 3456. [CrossRef] [PubMed]
10. Gaikadi, S.; Vasantha Kumar, S. Assessment of Urban Green Cover and its Types using Threshold-based Approach. *Int. J. Geoinformatics* **2024**, *20*, 74–85. [CrossRef]
11. Yang, X.; Chen, L.; Li, Y.; Xi, W.; Chen, L. Rule-based land use/land cover classification in coastal areas using seasonal remote sensing imagery: A case study from Lianyungang City, China. *Environ. Monit. Assess.* **2015**, *187*, 449. [CrossRef] [PubMed]
12. Alam, S.M.R.; Hossain, M.S. A Rule-Based Classification Method for Mapping Saltmarsh Land-Cover in South-Eastern Bangladesh from Landsat-8 OLI. *Can. J. Remote Sens.* **2021**, *47*, 356–380. [CrossRef]
13. Arpitha, M.; Ahmed, S.A.; Harishnaika, N. Land use and land cover classification using machine learning algorithms in google earth engine. *Earth Sci. Inform.* **2023**, *16*, 3057–3073. [CrossRef]
14. Arfa, A.; Minaei, M. Utilizing multitemporal indices and spectral bands of Sentinel-2 to enhance land use and land cover classification with random forest and support vector machine. *Adv. Space Res.* **2024**, *74*, 5580–5590. [CrossRef]
15. Zaraza Aguilera, M.A. Classification of land-cover through machine learning algorithms for fusion of sentinel-2A and planetscope imagery. *Int. Arch. Photogramm. Remote Sens. Spat. Inf. Sci.—ISPRS Arch.* **2020**, *XLII-3/W12-2020*, 361–368. [CrossRef]
16. Zhao, S.; Tu, K.; Ye, S.; Tang, H.; Hu, Y.; Xie, C. Land Use and Land Cover Classification Meets Deep Learning: A Review. *Sensors* **2023**, *23*, 8966. [CrossRef] [PubMed]
17. De Luca, G.; Silva, J.M.N.; Cerasoli, S.; Araújo, J.; Campos, J.; Di Fazio, S.; Modica, G. Object-based land cover classification of cork oak woodlands using UAV imagery and Orfeo Toolbox. *Remote Sens.* **2019**, *11*, 1238. [CrossRef]
18. Goodin, D.G.; Anibas, K.L.; Bezymennyi, M. Mapping land cover and land use from object-based classification: An example from a complex agricultural landscape. *Int. J. Remote Sens.* **2015**, *36*, 4702–4723. [CrossRef]
19. Zhang, C.; Sargent, I.; Pan, X.; Li, H.; Gardiner, A.; Hare, J.; Atkinson, P.M. Joint Deep Learning for land cover and land use classification. *Remote Sens. Environ.* **2019**, *221*, 173–187. [CrossRef]
20. Digra, M.; Dhir, R.; Sharma, N. Land use land cover classification of remote sensing images based on the deep learning approaches: A statistical analysis and review. *Arab. J. Geosci.* **2022**, *15*, 1003. [CrossRef]
21. Kamilaris, A.; Prenafeta-Boldú, F.X. Deep learning in agriculture: A survey. *Comput. Electron. Agric.* **2018**, *147*, 70–90. [CrossRef]
22. Xu, Y.; Huang, B. Spatial and temporal classification of synthetic satellite imagery: Land cover mapping and accuracy validation. *Geo-Spat. Inf. Sci.* **2014**, *17*, 1–7. [CrossRef]
23. Carneiro, G.F.; Ferreira, M.P.; de Sá Volotão, C.F. Multi-source remote sensing data improves the classification accuracy of natural forests and eucalyptus plantations. *Rev. Bras. Cartogr.* **2020**, *72*, 110–125. [CrossRef]
24. Chen, B.; Huang, B.; Xu, B. Multi-source remotely sensed data fusion for improving land cover classification. *ISPRS J. Photogramm. Remote Sens.* **2017**, *124*, 27–39. [CrossRef]
25. Du, P.; Xia, J.; Zhang, W.; Tan, K.; Liu, Y.; Liu, S. Multiple classifier system for remote sensing image classification: A review. *Sensors* **2012**, *12*, 4764–4792. [CrossRef] [PubMed]
26. Zhu, Z.; Gallant, A.L.; Woodcock, C.E.; Pengra, B.; Olofsson, P.; Loveland, T.R.; Jin, S.; Dahal, D.; Yang, L.; Auch, R.F. Optimizing selection of training and auxiliary data for operational land cover classification for the LCMAP initiative. *ISPRS J. Photogramm. Remote Sens.* **2016**, *122*, 206–221. [CrossRef]
27. Zanaga, D.; Van De Kerchove, R.; De Keersmaecker, W.; Souverijns, N.; Brockmann, C.; Arino, O. *ESA WorldCover 10 m 2020 v100*; Zenodo: Geneva, Switzerland, 2020.
28. Malinowski, R.; Lewiński, S.; Rybicki, M.; Gromny, E.; Jenerowicz, M.; Krupiński, M.; Nowakowski, A.; Wojtkowski, C.; Krupiński, M.; Krätzschmar, E.; et al. Automated production of a land cover/use map of Europe based on sentinel-2 imagery. *Remote Sens.* **2020**, *12*, 3523. [CrossRef]
29. European Environment Agency (EEA). *CORINE Land Cover 2018 (CLC2018)*, version 2020_20u1; Copernicus Land Monitoring Service; European Environment Agency (EEA): Copenhagen, Denmark, 2019.
30. De Fioravante, P.; Luti, T.; Cavalli, A.; Giuliani, C.; Dichicco, P.; Marchetti, M.; Chirici, G.; Congedo, L.; Munafò, M. Multispectral Sentinel-2 and SAR Sentinel-1 Integration for Automatic Land Cover Classification. *Land* **2021**, *10*, 611. [CrossRef]
31. Heymann, Y.; Steenmans, C.; Croisille, G.; Bossard, M. *CORINE Land Cover Technical Guide*; Office for Official Publications of the European Communities: Luxembourg, 1994.

32. Cilloccu, F.; Cumer, A.; Incollu, G. La Nuova Carta Dell'Uso del Suolo 1:25.000 Della Regione Sardegna. 2003. Available online: https://www.sardegnageoportale.it/documenti/6_83_20060201093458.pdf (accessed on 1 May 2026).
33. Sardegna Geoportale. Carta Dell'Uso del Suolo in Scala 1:25.000-2008. 2026. Available online: https://webgis2.regione.sardegna.it/geonetwork/srv/eng/catalog.search#/metadata/R_SARDEG:TVWIX (accessed on 19 May 2026).
34. Pungetti, G.; Marini, A.; Vogiatzakis, I. *Sardinia*; Springer: Dordrecht, The Netherlands, 2008; pp. 143–169. [CrossRef]
35. Camarda, I.; Laureti, L.; Angelini, P.; Capogrossi, R.; Carta, L.; Brunu, A. *Il Sistema Carta della Natura della Sardegna*; ISPRA: Roma, Italy, 2015.
36. Randazzo, G.; Cascio, M.; Fontana, M.; Gregorio, F.; Lanza, S.; Muzirafuti, A. Mapping of Sicilian Pocket Beaches Land Use/Land Cover with Sentinel-2 Imagery: A Case Study of Messina Province. *Land* **2021**, *10*, 678. [CrossRef]
37. Simonetti, D.; Marelli, A.; Eva, H. *IMPACT: Portable GIS Toolbox for Image Processing and Land Cover Mapping*; Publications Office of the European Union: Luxembourg, 2015.
38. Collu, C.; Simonetti, D.; Dessì, F.; Casu, M.; Pala, C.; Melis, M.T. A Multi-Temporal Sentinel-2 and Machine Learning Approach for Precision Burned Area Mapping: The Sardinia Case Study. *Remote Sens.* **2026**, *18*, 267. [CrossRef]
39. Mullissa, A.; Vollrath, A.; Odongo-Braun, C.; Slagter, B.; Balling, J.; Gou, Y.; Gorelick, N.; Reiche, J. Sentinel-1 SAR Backscatter Analysis Ready Data Preparation in Google Earth Engine. *Remote Sens.* **2021**, *13*, 1954. [CrossRef]
40. Pesaresi, M.; Schiavina, M.; Politis, P.; Freire, S.; Krasnodębska, K.; Uhl, J.H.; Carioli, A.; Corbane, C.; Dijkstra, L.; Florio, P.; et al. Advances on the Global Human Settlement Layer by joint assessment of Earth Observation and population survey data. *Int. J. Digit. Earth* **2024**, *17*, 2390454. [CrossRef]
41. Tolan, J.; Yang, H.I.; Nosarzewski, B.; Couairon, G.; Vo, H.V.; Brandt, J.; Spore, J.; Majumdar, S.; Haziza, D.; Vamaraju, J.; et al. Very high resolution canopy height maps from RGB imagery using self-supervised vision transformer and convolutional decoder trained on aerial lidar. *Remote Sens. Environ.* **2024**, *300*, 113888. [CrossRef]
42. Simonetti, D.; Pimple, U.; Langner, A.; Marelli, A. Pan-tropical Sentinel-2 cloud-free annual composite datasets. *Data Brief* **2021**, *39*, 107488. [CrossRef] [PubMed]
43. Simonetti, D.; Simonetti, E.; Szantoi, Z.; Lupi, A.; Eva, H.D. First Results From the Phenology-Based Synthesis Classifier Using Landsat 8 Imagery. *IEEE Geosci. Remote Sens. Lett.* **2015**, *12*, 1496–1500. [CrossRef]
44. Qian, Y.; Zhou, W.; Nytch, C.J.; Han, L.; Li, Z. A new index to differentiate tree and grass based on high resolution image and object-based methods. *Urban For. Urban Green.* **2020**, *53*, 126661. [CrossRef]
45. Boschetti, M.; Nutini, F.; Manfron, G.; Brivio, P.A.; Nelson, A. Comparative Analysis of Normalised Difference Spectral Indices Derived from MODIS for Detecting Surface Water in Flooded Rice Cropping Systems. *PLoS ONE* **2014**, *9*, e88741. [CrossRef] [PubMed]
46. Boschetti, M.; Busetto, L.; Manfron, G.; Laborte, A.; Asilo, S.; Pazhanivelan, S.; Nelson, A. PhenoRice: A method for automatic extraction of spatio-temporal information on rice crops using satellite data time series. *Remote Sens. Environ.* **2017**, *194*, 347–365. [CrossRef]
47. Collu, C.; Simonetti, D.; Dessì, F.; Naitza, L.; Lasio, P.; Botti, P.; Melis, M.T. Open Source Technologies for Mapping: Impact Toolbox and the Land Cover Map of Sardinia. In *Current Challenges and Opportunities for Environmental Monitoring*; Associazione Italiana Di Telerilevamento (AIT), Ed.; AIT Series "Trends in Earth Observation"; AIT: Firenze, Italy, 2024; Volume 3, pp. 70–73. [CrossRef]
48. Câmara, G.; Vinhas, L.; Ferreira, K.R.; Queiroz, G.R.; De Souza, R.C.M.; De Monteiro, A.M.V.; De Carvalho, M.T.; Casanova, M.A.; De Freitas, U.M. *TerraLib: An Open Source GIS Library for Large-Scale Environmental and Socio-Economic Applications*; Springer: Berlin/Heidelberg, Germany, 2008; pp. 247–270. [CrossRef]
49. Baatz, M.; Schäpe, A. Multiresolution segmentation: An optimization approach for high quality multi-scale image segmentation. In *Angewandte Geographische Informationsverarbeitung XII*; Wichmann-Verlag: Heidelberg, Germany, 2000; pp. 12–23.
50. Mallah, S.; Gorji, M.; Balali, M.R.; Asadi, H.; Davatgar, N.; Varmazyari, H.; Stellacci, A.M.; Castellini, M. Deep Insight on Land Use/Land Cover Geospatial Assessment through Internet-Based Validation Tool in Upper Karkheh River Basin (KRB), South-West Iran. *Land* **2023**, *12*, 979. [CrossRef]
51. Olofsson, P.; Foody, G.M.; Herold, M.; Stehman, S.V.; Woodcock, C.E.; Wulder, M.A. Good practices for estimating area and assessing accuracy of land change. *Remote Sens. Environ.* **2014**, *148*, 42–57. [CrossRef]
52. Card, D.H. Using known map category marginal frequencies to improve estimates of thematic map accuracy. *Photogramm. Eng. Remote Sens.* **1982**, *48*, 431–439.
53. Listiani, I.A.; Leloglu, U.M.; Zeydanli, U.; Caliskan, B.K. Mapping Mediterranean maquis formations using Sentinel-2 time-series. *Ecol. Inform.* **2022**, *71*, 101814. [CrossRef]
54. Puletti, N.; Chianucci, F.; Castaldi, C. Use of Sentinel-2 for forest classification in Mediterranean environments. *Ann. Silvic. Res.* **2018**, *42*, 32–38. [CrossRef]

55. Mahdavi, S.; Salehi, B.; Granger, J.; Amani, M.; Brisco, B.; Huang, W. Remote sensing for wetland classification: A comprehensive review. *GIScience Remote Sens.* **2018**, *55*, 623–658. [CrossRef]
56. Ludwig, C.; Walli, A.; Schleicher, C.; Weichselbaum, J.; Riffler, M. A highly automated algorithm for wetland detection using multi-temporal optical satellite data. *Remote Sens. Environ.* **2019**, *224*, 333–351. [CrossRef]

https://doi.org/10.3390/land15081461